Energy & Environmental Science

ROYAL SOCIETY OF CHEMISTRY

PAPER

View Article Online
View Journal

Cite this: DOI: 10.1039/d0ee01834a

pH swing cycle for CO_2 capture electrochemically driven through proton-coupled electron transfer†

Shijian Jin, [a] Min Wu, [a] Roy G. Gordon, [b] Michael J. Aziz *[a] and David G. Kwabi ‡[a]

Received 9th June 2020,
Accepted 16th September 2020

DOI: 10.1039/d0ee01834a

rsc.li/ees

We perform a thermodynamic analysis of the energetic cost of CO_2 separation from flue gas (0.1 bar CO_2(g)) and air (400 ppm CO_2) using a pH swing created by electrochemical redox reactions involving proton-coupled electron transfer from molecular species in aqueous electrolyte. In this scheme, electrochemical reduction of these molecules results in the formation of alkaline solution, into which CO_2 is absorbed; subsequent electrochemical oxidation of the reduced molecules results in the acidification of the solution, triggering the release of pure CO_2 gas. We examined the effect of buffering from the CO_2–carbonate system on the solution pH during the cycle, and thereby on the open-circuit potential of an electrochemical cell in an idealized four-process CO_2 capture-release cycle. The minimum work input varies from 16 to 75 kJ $mol_{CO_2}^{-1}$ as throughput increases, for both flue gas and direct air capture, with the potential to go substantially lower if CO_2 capture or release is performed simultaneously with electrochemical reduction or oxidation. We discuss the properties required of molecules that would be suitable for such a cycle. We also demonstrate multiple experimental cycles of an electrochemical CO_2 capture and release system using 0.078 M sodium 3,3′-(phenazine-2,3-diylbis(oxy))bis(propane-1-sulfonate) as the proton carrier in an aqueous flow cell. CO_2 capture and release are both performed at 0.465 bar at a variety of current densities. When extrapolated to infinitesimal current density we obtain an experimental cycle work of 47.0 kJ $mol_{CO_2}^{-1}$. This result suggests that, in the presence of a 0.465 bar/1.0 bar inlet/outlet pressure ratio, a 1.9 kJ $mol_{CO_2}^{-1}$ thermodynamic penalty should add to the measured value, yielding an energy cost of 48.9 kJ $mol_{CO_2}^{-1}$ in the low-current-density limit. This result is within a factor of two of the ideal cycle work of 34 kJ $mol_{CO_2}^{-1}$ for capturing at 0.465 bar and releasing at 1.0 bar. The ideal cycle work and experimental cycle work values are compared with those for other electrochemical and thermal CO_2 separation methods.

Broader context

CO_2 emission primarily from fossil fuel combustion is causing climate change at an alarming rate. Carbon capture and sequestration (CCS) has attracted R&D investment due to its potential to remove CO_2 from combustion exhaust. Although pilot-scale amine-based CCS at fossil-fired power plants has been demonstrated, the required heat input and the associated amine degradation and evaporative losses at elevated temperature may hinder its wide application. Here we present an electrochemically driven CO_2 separation approach that relies on a solution pH swing driven by the proton-coupled electron transfer (PCET) of small molecules, and requires electrical but no thermal input. Electrochemical reduction of these molecules de-acidifies an aqueous solution, which then absorbs CO_2; subsequent electrochemical oxidation of the reduced molecules acidifies the solution, triggering the release of pure CO_2 gas. Our analysis suggests the minimum electrical work input of this approach is 16–75 kJ $mol_{CO_2}^{-1}$, depending on the throughput, for both CO_2 separation from air and a typical flue gas with 0.1 bar CO_2. We demonstrate this approach experimentally using a flow cell with an aqueous-soluble phenazine-based electrolyte that undergoes PCET. The resulting energy cost of 47 kJ $mol_{CO_2}^{-1}$ in the low-current-density limit is compared to other methods.

[a] John A. Paulson School of Engineering and Applied Sciences, Harvard University, Cambridge, Massachusetts, 02138, USA. E-mail: maziz@harvard.edu
[b] Department of Chemistry and Chemical Biology, Harvard University, Cambridge, Massachusetts, 02138, USA

† Electronic supplementary information (ESI) available. See DOI: 10.1039/d0ee01834a

‡ Present address: Department of Mechanical Engineering, University of Michigan, Ann Arbor, MI 48109, USA, dkwabi@umich.edu

Introduction

Accumulating CO_2 emissions from the burning of fossil fuels[1] are resulting in an alarming rate of climate change. Consequently, there are increasing efforts worldwide to reduce societal reliance on fossil fuel-based energy and to switch to carbon-free sources such as nuclear, solar, wind and geothermal.[2] According to the

Intergovernmental Panel on Climate Change, average atmospheric CO_2 concentrations have to stay below roughly 500 ppm in order to avoid severe consequences of global warming (greater than 2 °C above pre-industrial era levels) and irreversibly deleterious changes to natural habitats and ecosystems that would threaten the viability of human civilization.[3] Given, however, that the global rate of transition to low-carbon sources is presently not nearly fast enough to avoid this threshold, other approaches are urgently required to deal with the problem of rising CO_2 concentrations.

Among the most promising of these is carbon capture and sequestration (CCS), in which CO_2 is separated from a point source[4] (*e.g.*, flue gas from a coal or natural gas power plant), compressed, and sequestered away from the atmosphere. A variant on this idea is direct air capture (DAC),[5] in which CO_2 is captured directly from ambient air, compressed and sequestered. These strategies recognize the continued use of fossil fuels while combating atmospheric CO_2 accumulation. In principle, the pure CO_2 obtained after separation can be converted back into chemical fuels with carbon-free energy, thus providing fuels without added CO_2 emissions; this is an active research area.

CO_2 separation from mixed gases is the most energetically demanding step of CCS, and much effort has gone into developing separation techniques that expend as little energy as possible per unit of CO_2 captured. Most well-developed means for doing so are "temperature-swing" cycles that involve contacting CO_2 with a strongly basic sorbent in an absorption process, and then heating the CO_2-rich sorbent to release pure CO_2 and regenerate the sorbent. The overall heat input required for sorbent regeneration in temperature-swing cycles, however, is high (>100 kJ $mol_{CO_2}^{-1}$) as compared to the minimum thermodynamic free energy requirement for carbon capture from air (20 kJ $mol_{CO_2}^{-1}$) or flue gas with 0.1 bar CO_2 (6 kJ $mol_{CO_2}^{-1}$).[6] It is worth noting that CCS from flue gas with a monoethanolamine (MEA)-based liquid sorbent would require roughly 30% of the heat energy produced by coal-powered plants from combustion to be consumed by carbon capture,[4] thereby making it unavailable for electricity production. Although the energy consumption of amine-based technologies has been improved with functionalized solvents,[7] amine blends,[8] water-lean systems[7,9,10] *etc.*, and several power plants with more than 1000 tonne CO_2/day uptake capacity have been demonstrated for post-combustion capture,[11,12] other limitations such as sorbent degradation, evaporative losses, toxicity, and corrosivity raise concerns for wide application.[9] As a result, other CO_2 capture sorbents and strategies are actively being explored both in fundamental research and industry.

The use of hydroxide (OH^-) in alkaline aqueous solutions to capture CO_2, in the reactions $OH^- + CO_2 \rightarrow HCO_3^-$ and, subsequently, $HCO_3^- + OH^- \rightarrow CO_3^{2-} + H_2O$, has received renewed interest in recent years as part of a viable separation approach. DAC using strongly alkaline (pH > 14) solution to absorb CO_2 in a high-surface-area contactor, followed by a chemical regeneration cycle that uses thermal energy to subsequently release it from solid carbonate precipitates,[13,14] has begun commercialization. This process has an energetic cost that is comparable to that of many temperature-swing-based processes, but its potentially low financial cost ($94–$232 per $tonne_{CO_2}$) for DAC makes practical application more feasible.[14]

Developing simple and low-cost CCS approaches that use alkaline solutions thus represents a substantial opportunity in emissions mitigation. In this paper, we study an electrochemically mediated CO_2 separation approach that uses a large electrochemically-induced swing in solution pH to absorb and release CO_2 and requires electrical but no thermal energy input.[15] This approach relies on the use of small molecules that undergo proton-coupled electron transfer (PCET) in aqueous solution. Electrochemical reduction/oxidation ("redox") of these molecules results in proton uptake/release, respectively,[16,17] resulting in changes in solution pH[18] which, if large enough, can cause CO_2 to be strongly absorbed at high pH and released at low pH.[19,20] The maximum achievable pH increases with the pK_a of the reduced form of the PCET-active redox couple, and its solubility.

There has been extensive research into organic molecules capable of PCET, in part because it is pivotal in many biological energy-conversion processes such as respiration and photosynthesis.[21] Quinone-based molecules that undergo $2H^+$, $2e^-$ PCET with fast kinetics are particularly ubiquitous in the field of aqueous organic redox-flow batteries (RFBs).[22–31] One major drawback in using quinones as reactants for CO_2 separation, however, is that they typically have pK_a values that are <13.0, and solubilities <1.0 M. 1,2-Benzoquinone-3,5-disulfonic acid (or its reduced form: tiron) is a rare exception in the latter category, with a reported solubility of >2.0 M in 1 M sulfuric acid, however its chemical instability in water[32] renders it unattractive for electrochemical CO_2 separation.

Aza-aromatic redox-active compounds[24] are potentially more promising in terms of both high solubility and pK_a. Although it does not participate in PCET for most of the 0–14 pH range, quinoxaline has been shown to have a solubility above 4.0 M in water and in weakly alkaline aqueous solution.[33] Some phenazines also participate in $2H^+$, $2e^-$ PCET up to at least pH 14. Wang *et al.*, have presented Pourbaix diagrams of 2-hydroxyphenazine (HP), 2-amino-3-hydroxyphenazine (AHP), and benzo[*a*]hydroxyphenazine-7/8-carboxylic acid (BHPC) with slopes of -57.9, -65.8 and -61 mV pH^{-1}, respectively, in 7–14 pH range.[34] However, although these molecules have high solubility (1.7 M for HP, 0.43 M for AHP and 1.55 M for BHPC) at pH 14, their low solubility in neutral solution (0.44 mM for HP, 0.57 mM for AHP and 16 mM for BHPC) prevents them from swinging the pH down to values <5 needed for an effective capture-release cycle. Phenazine dihydroxysulfonic acid (DHPS) has high solubility (1.8 M), and it is reasonably chemically stable (*i.e.*, decomposing at <1%/day).[35] We discuss and criticize a CO_2 capture/release system using DHPS in the Discussion section.

In this paper we carry out a thermodynamic analysis of the energetic cost of this electrochemical process and calculate the minimum required electrical energy input per mole of CO_2 for an ideal four-process cycle based on the potential difference between applied reduction and oxidation potentials *vs.* pH. The results show the ideal cycle work input for this scheme is 16–75 kJ $mol_{CO_2}^{-1}$, depending on the separation throughput per cycle, for capture from both flue gas and atmosphere. PCET with organic molecules that undergo kinetically rapid redox reactions is a promising

electrochemical basis for practicable CCS, as it may both reduce energetic losses and lower overall costs per ton of CO_2 separated, due to the potential low cost of these chemicals.

Experimentally, we demonstrate an electrochemical CO_2 capture and release system using 0.078 M sodium 3,3′-(phenazine-2,3-diylbis(oxy))bis(propane-1-sulfonate) (**DSPZ**) as the proton carrier in an aqueous flow cell. Multiple continuous cycles of CO_2 absorption and desorption at a steady 0.465 bar CO_2 partial pressure were performed at current densities of 40 to 150 mA cm^{-2}, and the net electrical work input of the cycle at each current density was measured. The electrical work input extrapolated to infinitesimal current, where ohmic, electron transfer and mass transport overpotentials should be eliminated, was 47.0 kJ $mol_{CO_2}^{-1}$. From these results, we estimate that, in the low-current-density limit, the cycle work for capturing from a CO_2 partial pressure of 0.465 bar and releasing into 1 bar CO_2 to be our measured energy cost of 47.0 kJ $mol_{CO_2}^{-1}$ plus the thermodynamic minimum work of 1.9 kJ $mol_{CO_2}^{-1}$, *i.e.*, 48.9 kJ $mol_{CO_2}^{-1}$, for concentrating the CO_2. This value may be compared with the ideal cycle work of 34 kJ $mol_{CO_2}^{-1}$ for the latter conditions. The results offer promise for further development and provide guidance on the design of future low energy electrochemical CCS devices. We also demonstrate, for the first time, a stable and multi-cycle electrochemical flow cell CCS device.

Thermodynamic analysis

In order to effect large changes in solution pH using PCET in aqueous media containing CO_2, buffering from inorganic carbon species must be overcome. Thus, we first examine the dependence of pH on the constituents of dissolved inorganic carbon (DIC) species present in solution, namely aqueous CO_2 (CO_2(aq)), bicarbonate (HCO_3^-) and carbonate (CO_3^{2-}):[36]

$$\mathrm{DIC} = [\mathrm{CO_2(aq)}] + [\mathrm{HCO_3^-}] + [\mathrm{CO_3^{2-}}] \quad (1)$$

The relative ratios of these species at equilibrium is dictated by the reactions between aqueous CO_2 and water:

$$\mathrm{CO_2(aq) + H_2O \overset{K_1}{\Leftrightarrow} HCO_3^- + H^+ \overset{K_2}{\Leftrightarrow} CO_3^{2-} + 2H^+} \quad (2)$$

where K_1 and K_2 are the first and second dissociation constants of carbonic acid (H_2CO_3), respectively, and defined as the following equilibrium constants:

$$K_1 = \frac{[\mathrm{HCO_3^-}][\mathrm{H^+}]}{[\mathrm{CO_2(aq)}]} \quad (3)$$

$$K_2 = \frac{[\mathrm{CO_3^{2-}}][\mathrm{H^+}]}{[\mathrm{HCO_3^-}]} \quad (4)$$

For a solution of zero salinity, K_1 and K_2 are 1.1×10^{-6} M and 4.1×10^{-10} M,[37] resulting in the first and second pK_a for carbonic acid being 6.0 and 9.4, respectively. Thus, in acidic solutions of pH < 6 total DIC is composed primarily of dissolved CO_2(aq), in basic solutions of pH > 9 total DIC is composed primarily of carbonate anions, and for the intermediate pH range total DIC is composed primarily of bicarbonate anions.[36] Because CO_2(aq), being uncharged, is the only form that exchanges with the atmosphere, increasing the pH of a solution drives down the activity of CO_2(aq), leading to net dissolution of CO_2(g) as CO_2(aq) and conversion to bicarbonate and/or carbonate. Correspondingly, decreasing the pH raises the activity of CO_2(aq), leading to outgassing. This provides a mechanism for selectively absorbing CO_2 from a mixture of gases, and then releasing a pure stream at a separate point for sequestration. Given that certain bicarbonate/carbonate compounds have exceptionally high solubilities (>3 M at room temperature) in water, this strategy affords a potential pathway for high-throughput separation of CO_2 from air or flue gas. Additionally, the fact that the entire process takes place in the liquid phase offers a potentially simpler and lower-cost CCS route as compared to schemes in which, having absorbed CO_2 using alkaline solution, precipitation and heating of solid carbonates is required to release gaseous CO_2.[13,14,38]

We envision a thermodynamic cycle comprising a series of alternating electrochemical and gas–liquid exchange processes: (1) electrochemical acidification of an electrolyte at constant DIC concentration, resulting in supersaturation of aqueous CO_2; (2) outgassing of pure CO_2 gas at the collection stream until gas–liquid equilibrium is reached; (3) electrochemical de-acidification of the electrolyte, resulting in strongly alkaline electrolyte; and (4) invasion of CO_2 from air/flue gas into the alkaline electrolyte. During each process, the constituents of DIC and pH can be described based on CO_2–carbonate and water dissociation equilibria, as well as the principle of charge conservation. Based on the definition of DIC set forth in eqn (1), the concentration of each component of DIC as a function of total DIC and $[H^+]$ is given by[36]

$$[\mathrm{CO_2(aq)}] = \frac{\mathrm{DIC}}{1 + \frac{K_1}{[\mathrm{H^+}]} + \frac{K_1 K_2}{[\mathrm{H^+}]^2}} \quad (5)$$

$$[\mathrm{HCO_3^-}] = \frac{\mathrm{DIC}}{1 + \frac{[\mathrm{H^+}]}{K_1} + \frac{K_2}{[\mathrm{H^+}]}} \quad (6)$$

$$[\mathrm{CO_3^{2-}}] = \frac{\mathrm{DIC}}{1 + \frac{[\mathrm{H^+}]}{K_2} + \frac{[\mathrm{H^+}]^2}{K_1 K_2}} \quad (7)$$

An additional constraint arises from the water dissociation equilibrium $\mathrm{H_2O \overset{K_w}{\Leftrightarrow} H^+ + OH^-}$ resulting in

$$[\mathrm{H^+}][\mathrm{OH^-}] = 10^{-14}\ \mathrm{M^2} \quad (8)$$

The total alkalinity (TA) of the solution under consideration is defined as[36]

$$\mathrm{TA} \equiv [\mathrm{OH^-}] + [\mathrm{HCO_3^-}] + 2[\mathrm{CO_3^{2-}}] - [\mathrm{H^+}] \quad (9)$$

Given the ionic species present, and assuming the electrolyte salt comprises cationic and anionic species S^+ and S^-, respectively, results in:

$$[\mathrm{S^+}] - [\mathrm{S^-}] = \mathrm{TA} \quad (10)$$

Eqn (10) follows from imposing a charge neutrality constraint in solution. It is important to note that PCET, involving the transfer of protons between a small molecule Q and solution, may directly change the solution TA. To understand this, consider the case of an electrochemical redox reaction such as $Q + e^- + xH^+ \leftrightarrow QH_x^{x-1}$ where x is the number of protons transferred per electron. To the extent that the satisfaction of charge neutrality following the reduction of Q is not fully accounted for by a change in DIC, $[H^+]$ or $[OH^-]$ content of the solution, it would result in a net increase in TA – *i.e.*, either *via* a transfer of S^- out of the solution or a transfer of S^+ into it. Likewise, oxidation of QH_x^{x-1} might yield a net decrease in TA. Changes in TA cause changes in pH; we stress, however, that TA and pH are not linearly related to each other: electrochemically induced perturbations to TA affect pH only subject to equilibria represented by eqn (5)–(9) being satisfied. In other words, PCET provides a driving force for pH swing through changing TA, but actual changes in pH depend on buffering from the CO_2–carbonate equilibrium.

We determine the minimum work required to separate CO_2 from a mixed gas stream using an electrically-driven pH-swing cycle involving these chemical and electrochemical processes. The four processes described above are represented schematically in Fig. 1, in which process 1 → 2 and 3 → 4 are constant DIC, electrochemical processes – associated with electrical energy input/output – whereas processes 2 → 3 and 4 → 1 involve gas–liquid exchange of CO_2 at open circuit potential and constant TA. All processes are assumed to be isothermal.

We first perform a preliminary calculation to determine the equilibrium TA at State 1, *i.e.*, after CO_2 invasion and before electrochemical acidification, for given values of DIC and CO_2 partial pressure. Fig. 2 shows the result of this analysis, in which solutions were found to the system of eqn (5)–(9) for two initial CO_2 partial pressures: 0.1 bar and 400 ppm CO_2(g), which correspond to the CO_2 concentration of flue gas from a typical coal power plant and atmospheric CO_2, respectively.

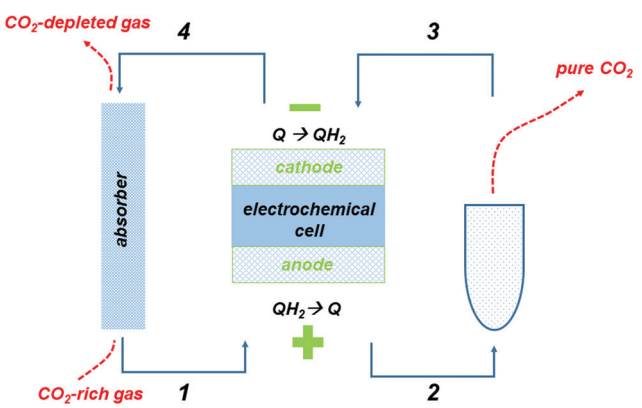

Fig. 1 Schematic of electrochemical CO_2 separation cycle, showing flow of liquid electrolyte (in blue lines) and gas (dashed red lines) between the electrochemical cell and gas–liquid exchange chambers, with various states numbered. Processes between numbered states are: electrochemical acidification (1 → 2), CO_2 outgassing (2 → 3), electrochemical de-acidification (3 → 4) and CO_2 invasion (4 → 1).

$[CO_2(aq)]$ is assumed to be fixed based on a Henry's Law constant of 35 mM/bar at room temperature. The results show that for both conditions, TA has an almost linear relationship to DIC, with DIC = 0.86 × TA at 0.1 bar CO_2(g), and 0.53 × TA at 400 ppm CO_2(g). Solution pH also increases with DIC, settling close to 8.6 in the limit of high DIC at 0.1 bar CO_2(g) (Fig. 2a) and 9.8 at 400 ppm CO_2 (Fig. 2b). An important reference point for these results is seawater in equilibrium with atmospheric CO_2, which mainly comprises HCO_3^- and is known to have a natural pH of about 8.1 for a DIC of ~2 mM.[36] Results in Fig. 2b are consistent with this expectation, as at a DIC of 2 mM the solution pH is 8.1.

We next consider the minimum concentration of PCET-active molecules required for process 1 → 2 *i.e.*, electrochemical acidification of the electrolyte at a fixed DIC. Fig. 3 shows the minimum concentration of a hypothetical small molecule capable of concerted $2H^+$, $2e^-$ PCET that is required to convert all DIC to CO_2(aq). CO_2 concentrations at the CO_2-rich gas inlet of 0.1 bar and 400 ppm were considered, and the TA at State 1 was calculated based on the relationship between DIC and TA shown in Fig. 2. Conversion of all carbonate/bicarbonate was deemed complete at the point where 99% of DIC is composed of CO_2(aq), after electrochemical acidification *via* QH_2 oxidation. For both inlet conditions, a linear relationship between DIC and minimum concentration of QH_2, or $[QH_2]_{min}$, was obtained, with $[QH_2]_{min}$ equal to 0.57 × DIC for the inlet with 0.1 bar CO_2, and 0.93 × DIC for that with 400 ppm CO_2, for DIC values in the range between 0 and 2.5 M.

We now calculate the minimum work input required to separate CO_2 in the ideal cycle defined above. As an example of a desirable implementation, we assume an inlet CO_2 partial pressure of 0.1 bar and a starting $[QH_2]$ of 1.4 M, which translates to a maximum convertible DIC of 2.46 M. The minimum work input is sensitive to two important parameters: the ratio of partial pressures of CO_2 at the exit to inlet stream, which we term the 'exit/inlet pressure ratio', and the CO_2 supersaturation at State 2, the start of outgassing. We define CO_2 supersaturation here as the ratio of $[CO_2(aq)]$ at the start of outgassing compared to equilibrium value of $[CO_2(aq)]$ at the exit. As the exit/inlet pressure ratio increases, the work of separation increases. CO_2 supersaturation at State 2, which we denote hereafter as 'outgassing overpressure', is proportional to CO_2 separation throughput as, for a given exit/inlet pressure ratio, it is a measure of how much dissolved CO_2 can be released in a single cycle. For the implementation under consideration, an exit/inlet pressure ratio of 10 was assumed (*i.e.*, 1 bar of pure CO_2(g) at the exit stream, for 0.1 bar inlet partial pressure), resulting in an outgassing overpressure of 69. Fig. 4a shows the pH of the solution as a function of Q concentration during electrochemical acidification, going from initial pH of 8.7 to 4.3 when complete conversion is achieved.

For the outgassing process 2 → 3 (Fig. 4a), eqn (5)–(9) are solved subject to the constraint that TA is fixed and, that at the end of the process, $[CO_2(aq)]$ relaxes to its equilibrium value at 1 bar of 35 mM. After this, process 3 → 4 (electrochemical de-acidification) is evaluated with DIC fixed at its value at State 3,

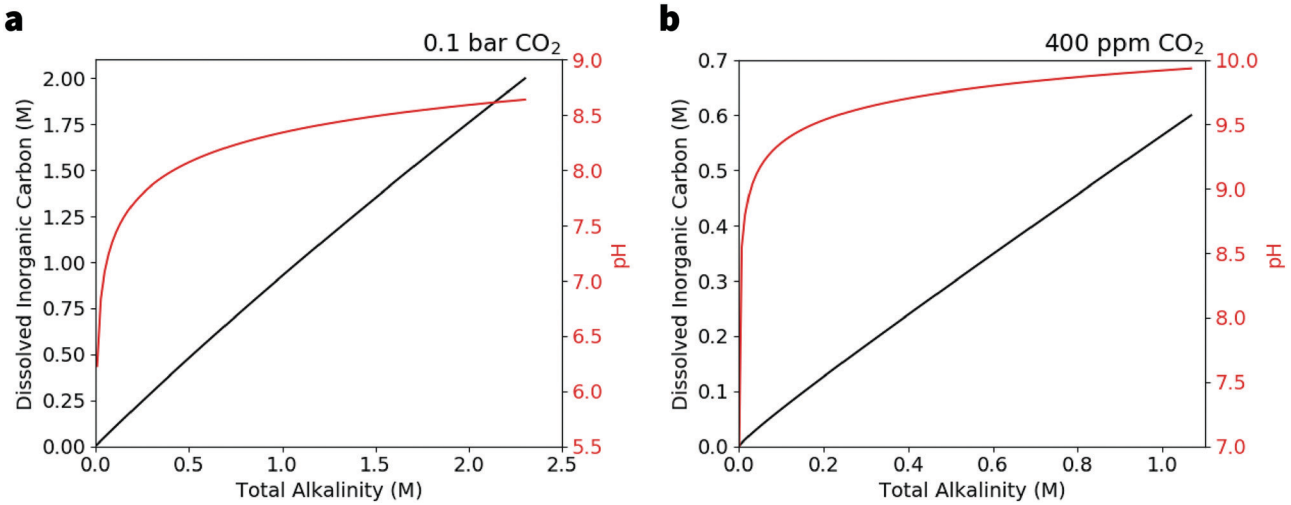

Fig. 2 DIC (black) and pH (red) as functions of TA at CO_2 partial pressures of (a) 0.1 bar and (b) 400 ppm.

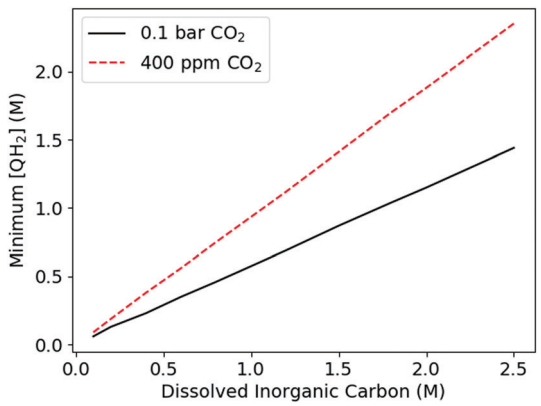

Fig. 3 Minimum concentration of QH_2 required to convert 99% of all DIC to CO_2(aq).

using parameters from State 3 as inputs (Fig. 4c); the pH goes from 6 to ~14.5 as the concentration of QH_2 increases. CO_2 invasion (Fig. 4d) then occurs, completing the cycle and restoring State 1. The relationship between DIC and pH throughout the cycle is shown in Fig. 5, whereas that between pH and [CO_2(aq)] is shown in Fig. S1 (ESI†). For comparison, an ideal cycle assuming a more moderate reactant solubility (*i.e.*, the lower of Q and QH_2 solubilities) of 0.1 M (resulting in DIC at State 1 of 0.175 M) is shown in Fig. S2 (ESI†). An important consequence of the lower solubility is that the pH after electrochemical de-acidification (process 3 → 4) is 13, rather than 14.5; this is a direct result of the lesser degree of de-acidification afforded by the removal of 0.2 M H^+ from solution, as opposed to 2.8 M H^+ (*i.e.*, assuming $2H^+$, $2e^-$ redox processes in both the 0.1 M and 1.4 M solubility cases). As will be discussed presently, the pH attained after the deacidification process 3 → 4 is an important metric that constrains the selection of viable molecules for electrochemical CCS. It is also important to note that based on the relationship between DIC value and minimum [QH_2] required for full acidification shown in Fig. 3, the concentration of QH_2 at State 1 constrains combinations of exit/inlet pressure ratio and outgassing overpressure that may be used in an ideal cycle. An illustration of this is given in Fig. S3 (ESI†), which shows lines of constant [QH_2] for different exit/inlet pressure ratios and outgassing overpressures. As expected, higher outgassing overpressures and exit/inlet pressure ratios require higher concentrations of starting [QH_2] to run a cycle.

In calculating the energetic cost per mole of CO_2 separated, we note that only processes 1→ 2 and 3 → 4 involve work inputs/outputs to or from the electrochemical cell, respectively. Using the Nernst equation and assuming dilute solutions, we relate the pH during each of those processes to the redox potential (E_R) of the electrode at which conversion between the pairs of the Q/QH_2 redox couple occurs: $E_R = E_0 - (59\ \text{mV} \times \text{pH})$ where E_0 is the redox potential under standard conditions, in which pH = 0.

Fig. 6 shows the result of this calculation for electrochemical acidification and de-acidification, where the area between the potential profiles represents the net electrical energy input. Dividing this area by the DIC released, *i.e.*, the absolute difference in DIC between states 1 and 3, yields the overall work input per mole of CO_2 captured, $\bar{w}$, which may be represented as follows:

$$\bar{w} = \frac{2F}{\Delta\text{DIC}} \oint E \mathrm{d}q \qquad (11)$$

Here, F is Faraday's constant of 96 485 C mol^{-1}, ΔDIC represents the difference in DIC before and after CO_2 outgassing, E is redox potential, and the factor of 2 results from the assumption that each Q/QH_2 species undergoes a 2-electron redox process. In the implementation under consideration, the net electrical work input is 50 kJ $mol_{CO_2}^{-1}$.

Following a program similar to that sketched out above, Fig. 7 shows the ideal cycle work input required for CO_2 separation from inlet streams with 0.1 bar CO_2 (Fig. 7a) and 400 ppm CO_2 (Fig. 7b), for exit/inlet pressure ratios that result in CO_2 release around 1 bar at a variety of outgassing

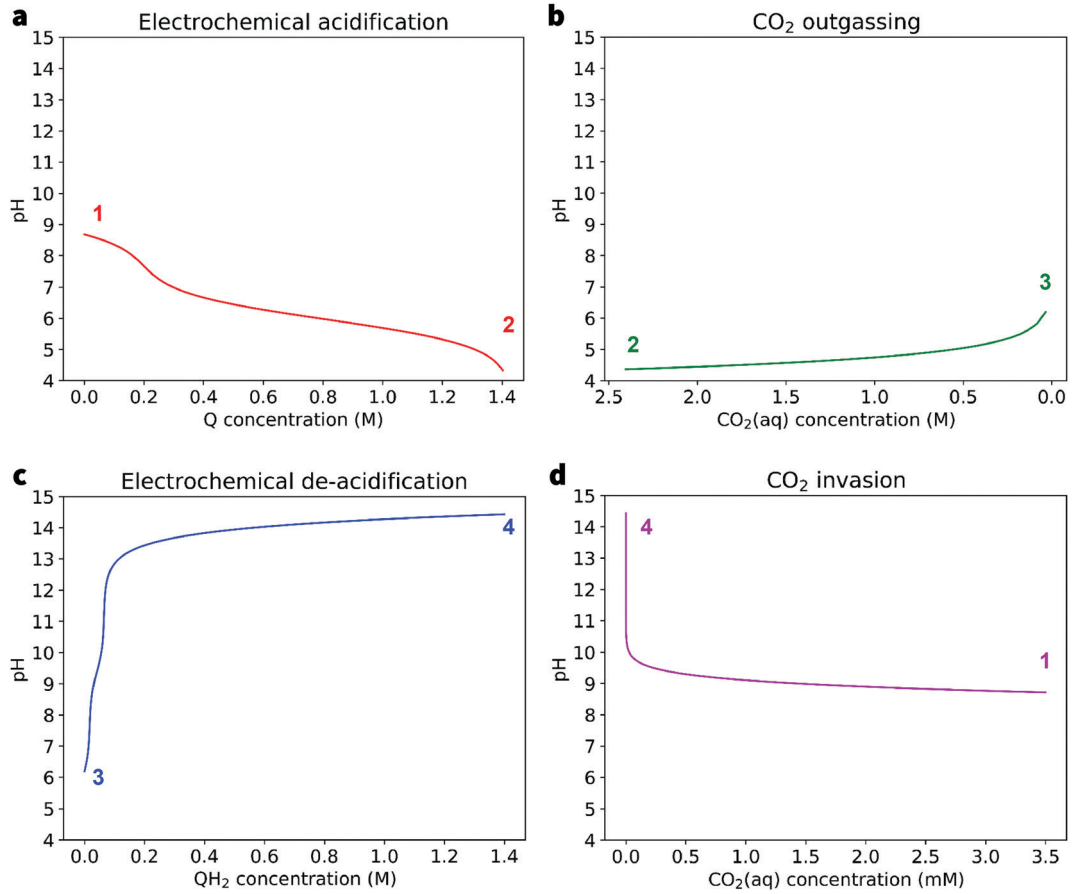

Fig. 4 pH as a function of Q, QH_2, and CO_2(aq) concentrations for an ideal CO_2 separation cycle with inlet and outlet CO_2(g) of 0.1 and 1 bar, respectively, during (a) electrochemical acidification (process 1 → 2, in red) (b) CO_2 outgassing at 1 bar CO_2(g) (process 2→ 3, in green) (c) electrochemical de-acidification (process 3 → 4, in blue) and (d) CO_2 invasion (process 4 → 1, in magenta), at the end of which aqueous CO_2 (CO_2(aq)) is assumed to be in equilibrium with 0.1 bar CO_2 gas. A starting value of [QH_2] of 1.4 M and a DIC value at State 1 of 2.46 M are assumed.

overpressures. Ideal cycle work is compared to the thermodynamic minimum work of separation required to provide the increase in CO_2 exergy, which, is directly related to the partial pressures of CO_2 at the inlet and exit streams:[4,6] $RT\ln(p_3/p_1)$, where R is the universal gas constant of 8.314 J mol^{-1} K^{-1} and temperature T is assumed to be 293.15 K (20 °C). For a given exit/inlet pressure ratio, the ideal cycle work input increases with outgassing overpressure, up to ∼ 50 and 75 kJ $mol_{CO_2}^{-1}$ for outgassing overpressures of 100 for inlets of 0.1 bar and 400 ppm CO_2(g), respectively. This is expected as a consequence of the fact that higher CO_2 super-/undersaturation during the outgassing and invasion processes, respectively, cause increasingly greater exergetic losses; these losses contribute to the difference in average pH, and thus redox potential, of the electrolyte during electrochemical acidification and de-acidification (Fig. 6).

In order to reduce exergetic losses – and thereby reduce the ideal cycle work input – one may consider performing CO_2 invasion and outgassing simultaneously with electrochemical acidification and de-acidification, respectively; this way, extremes in solution pH, and potential, are avoided. Exemplary applications of this strategy during electrochemical de-acidification and acidification are presented by the dashed lines in Fig. 5 and 6, where, for the cycle outlined in Fig. 4 (inlet 0.1 bar, exit 1.0 bar), processes 1 → 2 and 2 → 3 are combined into one two-stage acidification process: electrochemical acidification at constant DIC until [CO_2(aq)] reaches its equilibrium value at 1 bar CO_2(g) of 35 mM, followed by outgassing at constant [CO_2(aq)] until [Q] reaches 1.4 M. This results in a decrease in the ideal cycle work input from 50 to 42 kJ $mol_{CO_2}^{-1}$. A similar approach can be applied to processes 3 → 4 and 4 → 1, combining them into two-stage electrochemical de-acidification at constant DIC until [CO_2(aq)] is 3.5 mM, followed by CO_2 invasion at constant [CO_2(aq)] until [QH_2] reaches 1.4 M. As large exergetic losses during CO_2 invasion are avoided, this results in a reduction in the ideal cycle work from 50 kJ $mol_{CO_2}^{-1}$ to 14 kJ $mol_{CO_2}^{-1}$. Combining both strategies in one two-process cycle that features zero exergetic losses results in an ideal cycle work input of 5.7 kJ $mol_{CO_2}^{-1}$, which is equal to the thermodynamic minimum work input. In practice, however, this strategy would come at the cost of lower CO_2 separation throughput, as CO_2 outgassing/invasion kinetics increase with lower/higher pH values, respectively.[39] The use of homogeneous catalysts such as carbonic anhydrase[40–42] to speed up CO_2 invasion/outgassing kinetics may be one way of making such a cycle practical.

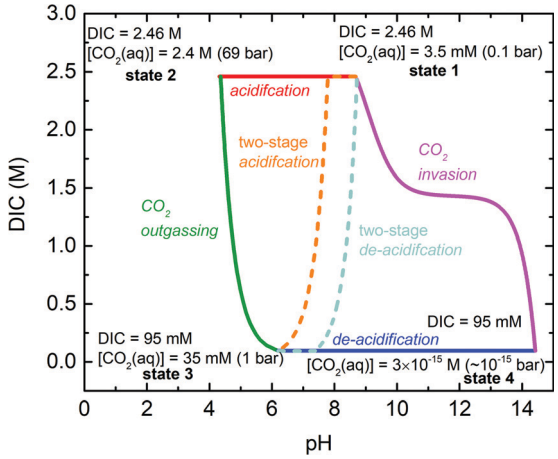

Fig. 5 DIC *vs.* pH during the 4-process cycle (solid lines) described in Fig. 4. At each numbered state, DIC, [CO_2(aq)], and equilibrium CO_2(g) corresponding to the value of [CO_2(aq)] are reported. The orange and cyan dashed lines refer to DIC *vs.* pH during two-stage acidification and de-acidification, respectively, in which electrochemical acidification and de-acidification are each performed in two stages: acidification at constant DIC up to [CO_2(aq)] = 35 mM, followed by outgassing and further acidification in tandem at constant [CO_2(aq)] until [Q] reaches 1.4 M; and de-acidification at constant DIC up to [CO_2(aq)] = 3.5 mM, followed by invasion and further de-acidification in tandem at constant [CO_2(aq)] until [QH_2] reaches 1.4 M.

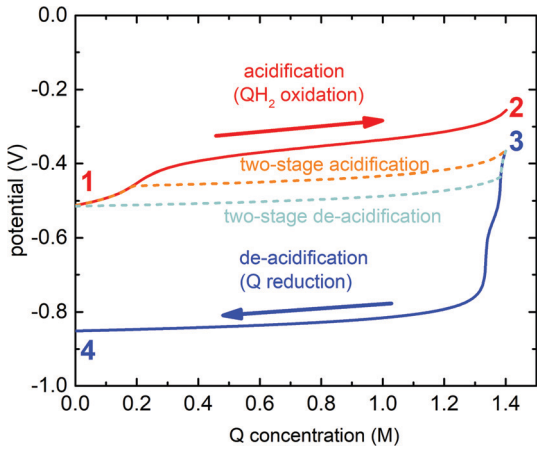

Fig. 6 Redox potential as a function of Q concentration during electrochemical acidification (red line, process 1 → 2) and de-acidification (blue line, process 3 → 4) for ideal CO_2 separation cycle of Fig. 5. The orange and cyan dashed lines refer to redox potential *vs.* Q concentration during two-stage acidification and de-acidification described in Fig. 5, respectively.

It is worth noting that CO_2 separation can, in principle, be run at arbitrarily high exit/inlet pressure ratios, and thus reach higher exit stream CO_2 partial pressures than indicated in Fig. 7. However, as already illustrated in Fig. S3 (ESI†), one would need increasingly higher concentrations of the PCET-active molecule, the solubility of which is constrained in reality (discussed in more detail below). Fig. S4 (ESI†) illustrates such a high-pressure exit stream case, where ideal cycle work is plotted *vs.* a series of exit/inlet pressure ratios, the highest of which yield CO_2 separation from either 0.1 bar or 400 ppm to 150 bar *i.e.*, approaching typical CO_2 pipeline pressures. Assuming an upper limit in QH_2 solubility of 10 M, our model predicts maximum achievable outgassing overpressures of approximately 3 and 2 for flue gas (Fig. S4a, ESI†) and DAC (Fig. S4b, ESI†), at work inputs of 40 and 70 kJ $mol_{CO_2}^{-1}$, respectively.

Several factors dictate the practical feasibility and optimal operation of an electrochemical CO_2 separation cycle based on the above scheme. With regard to a chosen redox pair Q/QH_2, high chemical stability in aqueous solution and fast redox kinetics are desirable for stable long-term operation and low activation losses. And, especially for CCS schemes in which oxygen composes a large fraction of the inlet gas composition (as in DAC), a high redox potential would be necessary to reduce or even eliminate the thermodynamic susceptibility of QH_2 to reversible chemical oxidation by O_2, which would cause an efficiency loss and possibly a cell electrolyte imbalance as well.

The most important attribute of Q, however, has to do with the highest pH it can effect upon being reduced during electrochemical de-acidification, as this determines the maximum value of DIC that can be deployed in a full CCS cycle and thus, the maximum CO_2 separation throughput per cycle. Higher values of DIC entail higher outgassing overpressures, which will require higher pH values to be achieved after electrochemical de-acidification. A DIC of 2.46 M enables an overpressure of ~70 given an exit pressure of 1 bar – *i.e.*, 70–2.46 M/0.035 M – but a final pH after de-acidification of 14.5 is required (Fig. 4c). However, a DIC of 0.175 M enables an overpressure of 5 (0.175 M/0.035 M), but requires a final pH upon de-acidification of only 13 (Fig. S2c, ESI†). In the ideal cycle under consideration, the hypothetical redox pair is considered capable of concerted $2H^+$, $2e^-$ PCET at all pH values, however in real aqueous solutions, PCET would be strongly affected by the affinity of the reduced reactant for protons. A common measure of this proton affinity is the pK_a of the protonated form of the reduced reactant, which is calculated based on the equilibrium between its protonated and deprotonated variants. A simplified reaction equation representing this equilibrium is:

$$QH_2 \leftrightarrow Q^{2-} + 2H^+ \quad (12)$$

Here, the equilibrium constant for this reaction is $K_a = [Q^{2-}][H^+]^2/[QH_2]$; and the p$K_a$ is defined as the logarithmic constant, $-\log_{10}K_a$. As this equilibrium is highly sensitive to solution acidity, increasingly basic solutions will favor the formation of the Q^{2-} rather than QH_2, in which case reduction of Q will not result in solution de-acidification as assumed. Based on the pK_a values and the water dissociation equilibrium, as well as the conservation of the total concentration of the molecule in all redox states, the ideal relationship between pK_a, Q concentration (*i.e.*, concentration of the oxidized form of the molecule) and final pH was derived, and is depicted in Fig. S5 (see ESI† Section: estimation of final pH after electrochemical de-acidification). As expected, the final pH scales strongly with pK_a, but is limited at low Q/QH_2 solubilities. As an illustration, consider a solution of Q with pK_a 15 – at a concentration of 50 mM, it will reach only pH 13 (equivalent to 100 mM OH^-) upon bulk electrolytic

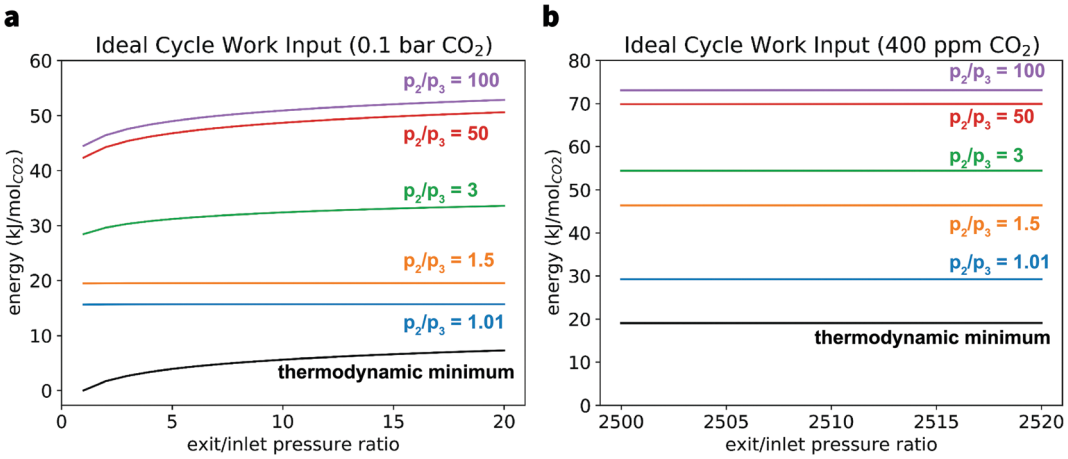

Fig. 7 Ideal cycle work as a function of the exit/inlet pressure ratio, p_3/p_1, for various values of the outgassing overpressure, p_2/p_3, for inlet streams of (a) 0.1 bar CO_2 and (b) 400 ppm CO_2. Exit/inlet pressure ratios around 2500 are plotted as this is relevant to DAC, where CO_2 is separated from 400 ppm to 1 bar. Both measures are compared against the minimum work of separation at each exit/inlet pressure ratio.

reduction, but will achieve a pH of 14.7 for a Q concentration of 4.0 M. Finding redox-active species with a combination of high solubility and high pK_a is therefore critical for reaching high DIC values in the electrochemical cycle, and thereby enabling high-throughput CO_2 separation.

Although DIC values greater than 3 M can, in principle, be attained in aqueous solution (room-temperature solubilities of $NaHCO_3$, Na_2CO_3, $KHCO_3$ and K_2CO_3 in water are 1.14, 3.2, 3.3 and 8.1 M, respectively[43,44]), solubilities of molecules capable of undergoing PCET across a wide pH range are typically lower, and thus limit DIC values that can be utilized in an electrochemical CCS cycle. Molecules with high reduction potential, high value of pK_a, high solubility and high chemical and electrochemical stability are necessary for practical electrochemical CCS devices.

Besides the choice of molecules, another critical question bearing on the practical implementation of this scheme relates to the nature of the electrochemical cell, and how it is integrated with CO_2 capture and release. Maximizing the overall energy efficiency of the system would require minimizing charge transport losses by using thin membranes with high perm-selectivity, minimizing activation losses by using catalytically active high-surface-area electrodes and redox-active species with fast kinetics, and minimizing mass transport/fluid pumping losses by using carefully engineered electrode pore structures[45,46] and flow fields.[47–51] In Fig. 1 it is assumed that these processes occur in steady-state: the electrolyte flows between an air contactor[38,52] at the inlet, where CO_2 absorption occurs at high pH; an electrochemical cell where acidification/deacidification take place; and the exit, where CO_2 is released at low pH. In order to maintain this pH differential across the cell membrane, it would be critical to have an ion-selective membrane that would strongly suppress the permeation of any ions that affect the solution TA (*i.e.*, ions on the right hand side of eqn (9)). A combination of an anion exchange membrane (AEM) and a cation exchange membrane (CEM) may be necessary to maintain a steady-state pH differential over a long period of time (Fig. S7, ESI†), as demonstrated for electrochemical water desalination by Desai *et al.*[53] In the next section, we demonstrate an electrochemical CCS flow cell using a **DSPZ** electrolyte. An inexpensive sulfonated hydrocarbon based CEM Fumatech E-620(K) was used as the membrane.

Experiment

We designed **DSPZ** to serve as the proton carrier because of its facile synthesis, high stability and quasi-reversible redox activity in a wide range of pH. **DSPZ** was synthesized through two simple steps using inexpensive materials and solvents with an overall yield of 67% as shown in Fig. 8a. The nuclear magnetic resonance spectrum of **DSPZ** is in Fig. S7 (ESI†). The solubility values of **DSPZ** in 1 M KCl (pH = 5.9) and 1 M KOH (pH = 14) were determined by UV-vis spectroscopy, and the values were both 0.73 M. (Fig. S8, ESI†).

Fig. 8b shows that **DSPZ** undergoes quasi-reversible electrochemistry at pH 3, 9 and 14, and the reduction potentials at these pH values are 0.05, −0.18 and −0.61 V *vs.* SHE, respectively. These results suggest a fitted slope of −59.5 mV pH^{-1}, indicating 2H$^+$, 2e$^-$ process throughout most of the pH range from 3 to 14. Its high solubility and wide functional pH range for PCET means that **DSPZ** satisfies our need for electrochemical CO_2 capture and release using a pH swing cycle.

To fully understand the pH evolution during deacidification and acidification, we constructed a flow cell capacity-limited by a negolyte of volume 7 mL with 0.1 M **DSPZ**. Both negolyte and posolyte were purged with and blanketed by nitrogen before and throughout the experiments, respectively, to avoid oxidation of reduced **DSPZ** by atmospheric oxygen. A schematic of the flow cell is shown in Fig. 9. We performed galvanostatic deacidification/acidification at 50 mA cm^{-2}, with potential holds at 1.65 V and 0.2 V at the end of each deacidification or acidification half cycle until current dropped to 10 mA cm^{-2} in order to utilize the full capacity (Fig. 8c). The pH of the **DSPZ**

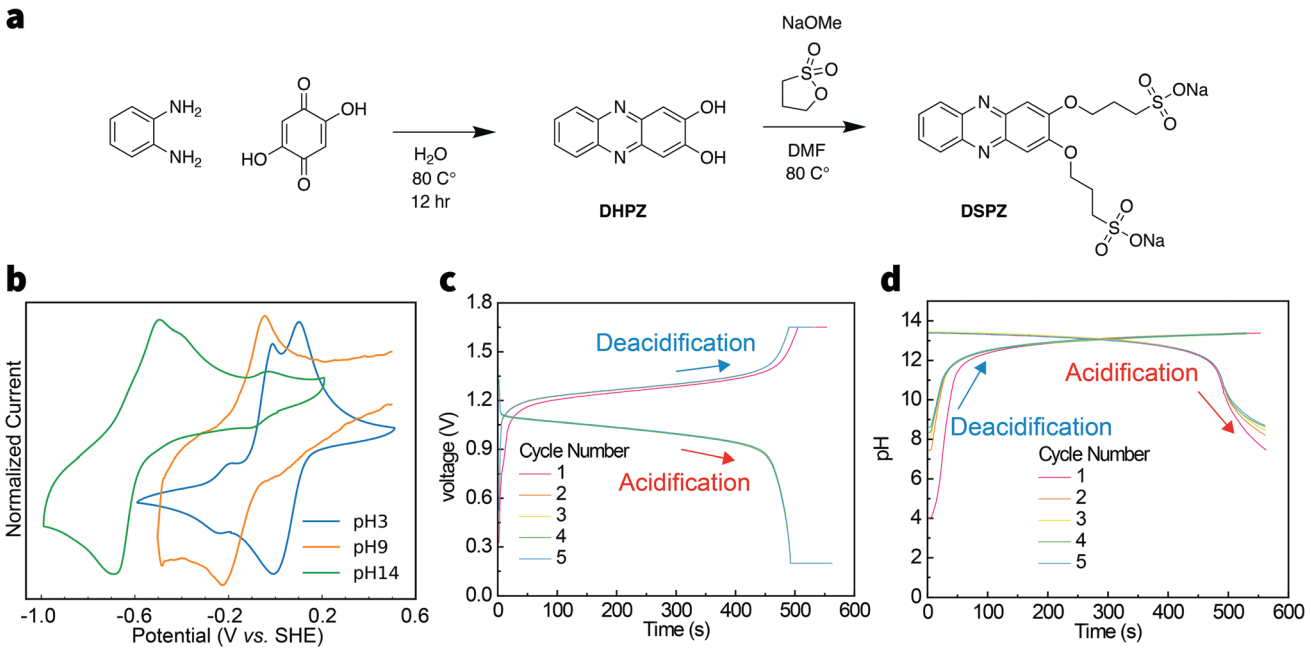

Fig. 8 Synthesis and electrochemical properties of **DSPZ**. (a) Synthetic scheme of **DSPZ**. (b) CV of 5 mM **DSPZ** at pH 3, 9 and 14 buffered 1 M KCl solutions. We attribute the small peaks near −0.2 V and −0.05 V *vs.* SHE in the pH 3 and 14 voltammograms, respectively, to a small amount of impurities. (c) Five cycles of galvanostatic deacidification and acidification at 50 mA cm^{-2} of the flow cell that comprised 7 mL 0.1 M **DSPZ** in 1 M KCl as negolytes (negative electrolyte) and 25 mL 0.1 M $K_4Fe(CN)_6$ 0.04 M $K_3Fe(CN)_6$ in 1 M KCl as posolyte (positive electrolyte). Potentiostatic holds at 1.65 V and 0.2 V were applied at the end of deacidification and acidification, respectively, to ensure high capacity utilization. (d) Reversible pH swings during the five cycles in (c).

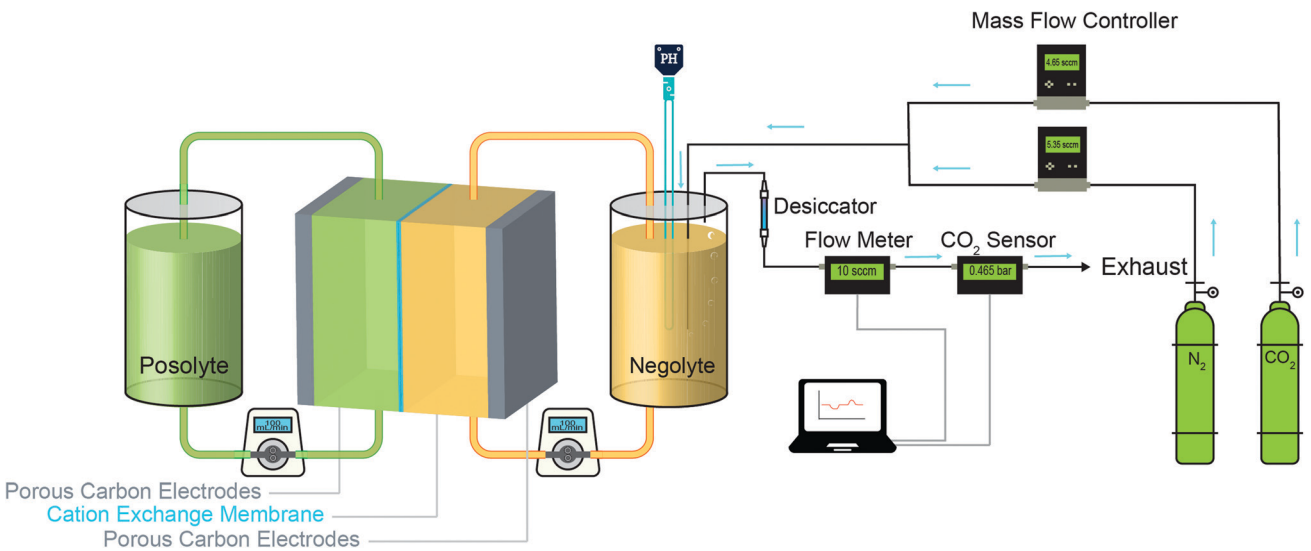

Fig. 9 Scheme of $Fe(CN)_6$ (posolyte)|**DSPZ** (negolyte) flow cell for CO_2 capture/release experiments. The blue arrows indicate gas flow.

negolyte was simultaneously recorded during deacidification/acidification cycles using a pH probe immersed in the negolyte solution (Fig. 8d).[27,28] In order to understand the electrochemistry of DSPZ in slightly acidic conditions, the initial pH was adjusted to 4.0 by adding a small amount of HCl solution. In the first full cycle, the pH increased from 4.0 to 13.4 during deacidification and returned from pH 13.4 to 7.5 during acidification, and the pH continued to cycle reversibly over the remaining four cycles. These results show that the electrochemical reactions of 0.1 M of **DSPZ** can swing the pH to >13 as predicted by Fig. S5 (ESI†), and the molecules can be cycled over a wide pH range of 4.0 to 13.4. The slight increase in pH over time at the end of acidification was likely caused by residual oxygen in our system, as evident by the <100% coulombic efficiency of the first cycle.[27] The close to 100% capacity utilization and the degree of pH change once again confirmed the $2H^+/2e^-$ redox process of **DSPZ**, which makes it a

suitable proton carrier for electrochemical CO_2 capture/release using a pH swing cycle.

To further explore the possibility of using **DSPZ** flow cell for CO_2 capture/release and compare to the ideal cycle shown in Fig. S2 (ESI†), we performed cycling of **DSPZ** in a steady mixed N_2/CO_2 environment with CO_2 partial pressure of 0.465 bar. The scheme of the setup is shown in Fig. 9. The inlet CO_2 and N_2 flow rates were controlled by mass flow controllers connected to each gas cylinder, and the two gases were mixed before entering the electrolyte chamber. At the gas outlet, the total gas flow rate and CO_2 partial pressure were measured using a digital flowmeter and a CO_2 sensor, respectively. The product of CO_2 partial pressure and the total flow rate gives the CO_2 flow rate.

Fig. 10 presents time series data over a full CO_2 capture and release cycle. The cell voltage profile, current density and pH were collected by the potentiostat while the CO_2 partial pressure and the total gas flow rate were simultaneously recorded by the CO_2 sensor and the flowmeter at the gas outlet. The initial CO_2 partial pressure was set to be 0.465 bar and the gas flow rate was set to be 10 mL min^{-1} (Fig. 10f). In this cycle, deacidification at 50 mA cm^{-2} started ~20 minutes after the start of the experiment (Fig. 10b). Both the cell voltage (Fig. 10a), and negolyte pH (Fig. 10d) increased due to the PCET reaction. We also estimated the increase in negolyte TA during deacidification assuming only K^+ ions crossed the CEM (Fig. 10c). When the cell voltage reached 1.65 V, the cell was turned to potentiostatic mode in order to continue deacidifying the electrolyte until the current dropped to 10 mA cm^{-2}, to enhance capacity utilization. A capacity utilization of 97.9% was achieved with this method. CO_2 absorption occurred simultaneously with deacidification, signified by a drop in outlet CO_2 partial pressure (Fig. 10e) and a pH drop as CO_2 reacts with OH^- to form CO_3^{2-}/HCO_3^-. The absorption period lasted ~40 minutes beyond the end of charging process, presumably

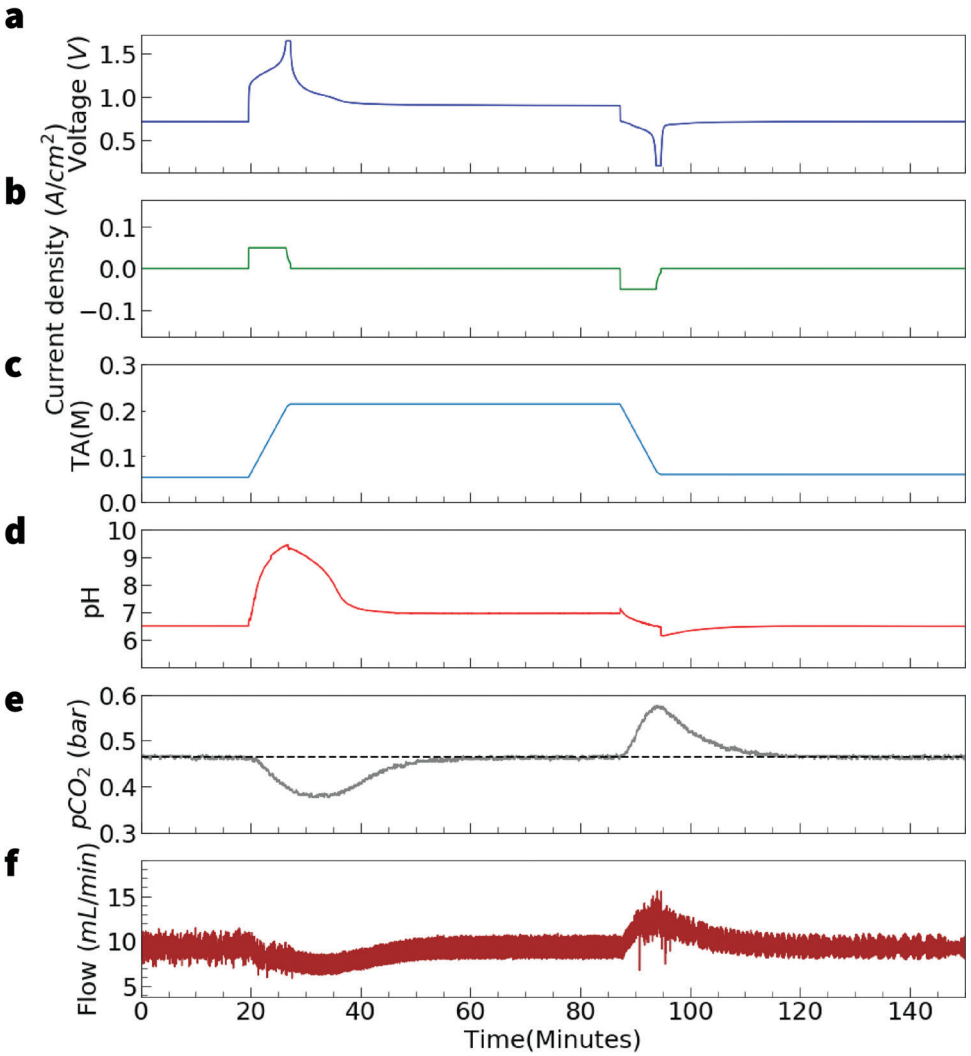

Fig. 10 One full CO_2 capture and release cycle with **DSPZ** based flow cell. Electrolytes comprised 7 mL 0.078 M **DSPZ** in 1 M KCl (negolyte, capacity limiting side, theoretical capacity = 105.4 C) and 40 mL of 0.1 M $K_4Fe(CN)_6$ and 0.1 M $K_3Fe(CN)_6$ in 1 M KCl (posolyte, non-capacity limiting side) (a) Voltage profile. (b) Current density. (c) Estimated total alkalinity. (d) pH. (e) CO_2 partial pressure. The black dashed line indicates the 0.465 bar baseline. (f) Total gas flow rate.

due to sluggish CO_2 absorption kinetics at low pH; it ended 80 minutes after the start of the experiment, as indicated by the recovered CO_2 partial pressure at 0.465 bar and a steady pH value. The volume of absorbed CO_2 was obtained by integrating over time the product of CO_2 partial pressure, which can be translated to CO_2 percentage assuming 1 bar of total pressure, and the total gas flow rate, and subtracting the integration of the product of baseline CO_2 partial pressure and the total gas flow rate, *i.e.*

$$Q_{CO_2} = \sum_{n=t_i}^{t_f} \left(pCO_2^{base} - pCO_2^n\right) \dot{V}^n \Delta t \qquad (13)$$

where Q_{CO2} is the amount of CO_2 absorbed, t_i is the start time, t_f is the final time, pCO_2^{base} is the baseline CO_2 partial pressure, pCO_2^n is the measured CO_2 partial pressure (in bar) at the nth data recording time t_n, $\dot{V}^n$ is the total gas flow rate at time t_n and Δt is the time difference between successive measurements. The absorbed volume of CO_2 was calculated to be 26.6 mL or, assuming T = 293.15 K, P = 1 bar and ideal gas behavior resulting in a DIC increase during CO_2 invasion of 0.158 M (1.11 mmol CO_2 in 7 mL solution). Adding this ΔDIC to the existing DIC (0.073 M) before the deacidification, which can be calculated using the pH and pCO_2 before deacidification, the total DIC is 0.231 M at the end of the deacidification process. The measurement implies that the TA concentration at the end of CO_2 invasion is 0.216 M. During the deacidification process, each **DSPZ** molecule gains two electrons and two protons, and, under ideal conditions, two potassium ions will cross over from the posolyte to balance the charge, resulting a net increase in $[S^+]$ that is twice the **DSPZ** concentration (eqn (10)). The total **DSPZ** concentration is 0.078 M, so the expected ΔTA value is 0.156 M, resulting in a final expected TA of 0.213 M (after adding existing TA of 0.057 M) at the end of the deacidification process. The measured TA of 0.216 M is within 2% of the expected value for a TA of 0.213 M, suggesting that crossover of non-conservative ions (H^+, OH^- and non-CO_2 DIC) is negligible during deacidification/capture. The steady-state pH at the end of the absorption period was 7.0 (Fig. 10d), which is similar to the predicted value of 7.1 for 0.465 bar at TA of 0.213 M, considering the ±0.25 error bar of the pH probe. The similarity between theory and experimental results is reassuring. Acidification began after the completion of the absorption period around 83 minutes after the start of the experiment. The pH first dropped to 6.1 because of PCET releasing protons into solution and then increased to 6.5 because of DIC turning into gaseous CO_2. pH, CO_2 partial pressure and flow rate measurements all show that the previously absorbed ΔDIC turned completely to gaseous CO_2 ~40 minutes after the start of acidification (Fig. 10d–f). The desorbed CO_2 amount, calculated using the negative of the right-hand side of eqn (13), was 26.3 mL, which is within 2% of the absorbed amount. The net electrical work of the full cycle is calculated by subtracting the work returned during acidification from the work input during deacidification, *i.e.*

$$w_{cycle} = w_{deacidification} - w_{acidification} \qquad (14)$$

where $w_{deacidification/acidification}$ can be calculated by:

$$w_{deacidification/acidification} = \sum_{n=t_i}^{t_f} |V^n j^n A| \Delta t \qquad (15)$$

where V^n is the cell voltage at the nth data recording time t_n, j^n is the current density at time t_n and A is the active geometric area of 5 cm^2. We take the absolute value, recognizing the direction of the work interactions through the minus sign in eqn (14). Work returned during acidification can be calculated similarly. In this cycle, $w_{deacidification}$ is 0.14 kJ and $w_{acidification}$ 0.063 kJ, so the cycle work is 0.08 kJ. Considering 1.11 mmol absorbed/desorbed CO_2, the total work per mole is 72.1 kJ mol_{CO2}^{-1}. This energy is high because the ohmic, electron transfer and mass transport overpotentials are high at this current density of 50 mA cm^{-2}.[54]

In order to understand how the CO_2 capture capacity and net electrical work depend on current density, we performed the same experiment at different current densities. Fig. 11 shows five cycles each, at current densities of 40, 50, 75, 100, 125 and 150 mA cm^{-2}, performed using the same cell and electrolyte compositions as for the one-cycle experiment reported in Fig. 10. Across different current densities, the amount of absorbed/desorbed CO_2 remained the same, at an average value of 26.7 mL or, with the same assumptions as above, 0.159 M ΔDIC (1.11 mmol CO_2, Fig. 12a). The same amount of absorbed CO_2 is reasonable because the cell capacity and estimated TA after deacidification remained the same, regardless of current density, and a potentiostatic hold was applied at the end of each half cycle in order for the measured capacity to approach the theoretical value. The energy consumption, however, is a different story because ohmic, electron transfer and mass transport overpotentials increase monotonically with increasing current density. Fig. 12b reports the dependence upon current density of the electrical work consumed and returned by the system; their difference is the net electrical work w_{cycle}. For the cycles under 0.465 bar CO_2, a linear extrapolation to 0 mA cm^{-2}, where ohmic and mass-transport overpotentials are expected to be negligible, suggests that the minimum electrical work input would be 47.0 kJ $mol_{CO_2}^{-1}$. Five cycles at each current density were also performed using the same cell with N_2 but no CO_2 in the headspace, and the resulting intercept shows that the minimum electrical work input is 32.0 kJ $mol_{CO_2}^{-1}$.

Fig. S9 (ESI†) demonstrates a CO_2 capture/release cycle in which CO_2 is concentrated from an inlet of 0.465 bar CO_2(g) to an exit of 1 bar using a flow cell with 0.09 M **DSPZ** negolyte. Because of transient changes in pCO_2 and gas flow rate, uncertainties accumulate in calculating the amount of CO_2 absorbed/released based on eqn (13). Instead, we estimated DIC values based on pH values, TA and eqn (5)–(10). At 40 mA cm^{-2}, the work input associated with this CO_2 separation cycle is between 79.3 and 84.2 kJ $mol_{CO_2}^{-1}$ (see ESI† Section: CO_2 capture from 0.465 bar and release to 1 bar).

Discussion

We interpret the value 47.0 kJ $mol_{CO_2}^{-1}$ (Fig. 12b) as being caused by electrode kinetic losses and exergetic losses that do

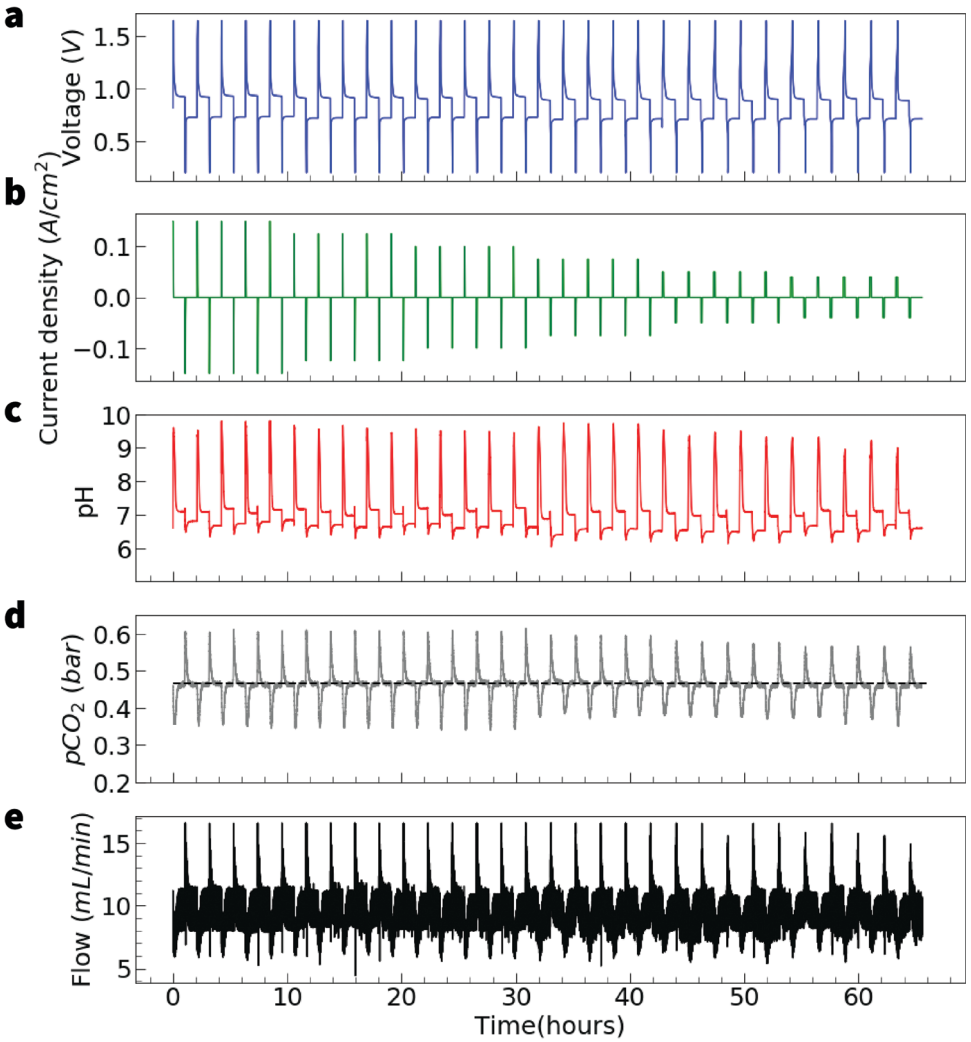

Fig. 11 Thirty full CO_2 capture and release cycles with a **DSPZ**-based flow cell at 40 to 150 mA cm^{-2}. Electrolytes comprised 7 mL 0.078 M **DSPZ** in 1 M KCl (negolyte, capacity limiting side, theoretical capacity = 105.4 C) and 40 mL of 0.1 M $K_4Fe(CN)_6$ and 0.1 M $K_3Fe(CN)_6$ in 1 M KCl (posolyte, non-capacity limiting side) (a) Voltage profile. (b) Current density. (c) pH. (d) CO_2 partial pressure. The black dashed line indicates the 0.465 bar baseline. (e) Total gas flow rate.

not disappear when extrapolated to zero current density. The former may mainly comprise activation overpotentials for electrochemical processes that often cause nonlinear behavior at low current density, *e.g.*, in fuel cells.[55] In our case, the work input associated with activation overpotentials is equivalent to the minimum electrical work input for cycling under N_2 demonstrated in Fig. 12b, *i.e.*, 32.0 kJ $mol_{CO_2}^{-1}$ because the same cell build and electrolyte composition were used. This value is twice the amount of our estimate of 15.7 kJ $mol_{CO_2}^{-1}$, calculated from the reported kinetic constants and transfer coefficients for a similar phenazine and ferrocyanide. (see ESI† Section: estimate of activation overpotential). We interpret the 15 kJ $mol_{CO_2}^{-1}$ gap between the measured minimum electrical work input in 0.465 bar CO_2 of 47.0 kJ $mol_{CO_2}^{-1}$ and that in N_2 of 32.0 kJ $mol_{CO_2}^{-1}$ as comprising exergetic losses caused by finite CO_2 absorption/desorption kinetics. Due to the behavior observed in Fig. 11a, b, d and 12a, we do not believe these exergetic losses varied significantly within the range of current densities accessed in our experiments. The next paragraph discusses the exergetic losses in detail. We expect an additional thermodynamic energy cost of 1.9 kJ $mol_{CO_2}^{-1}$ when a 0.465 bar/1.0 bar inlet/outlet pressure ratio exists. Therefore, when a 0.465 bar CO_2 source is concentrated to 1 bar using this cycle, the estimated experimental cycle work would be 48.9 kJ $mol_{CO_2}^{-1}$. This value may be compared with the ideal cycle work predicted by our thermodynamic analysis of the four-process cycle, *i.e.*, 34 kJ $mol_{CO_2}^{-1}$ for absorption from 0.465 bar and release to 1.0 bar (see ESI† Section: estimate of CO_2 kinetics losses).

The above calculation yielding 34 kJ $mol_{CO_2}^{-1}$, however, assumes a four-process CO_2 separation cycle, whereas the experimental situation is arguably closer to the two-process cycle, in which CO_2 release/invasion and acidification/de-acidification occur simultaneously. The two-process ideal cycle work would be the same as the thermodynamic minimum work, *i.e.*, 0 kJ $mol_{CO_2}^{-1}$ for the case of capturing from and releasing to the same environment, and 1.9 kJ $mol_{CO_2}^{-1}$ for capturing from 0.465 bar and releasing to 1 bar. It does not include exergetic losses that occur during an actual experimental cycle. We may estimate the

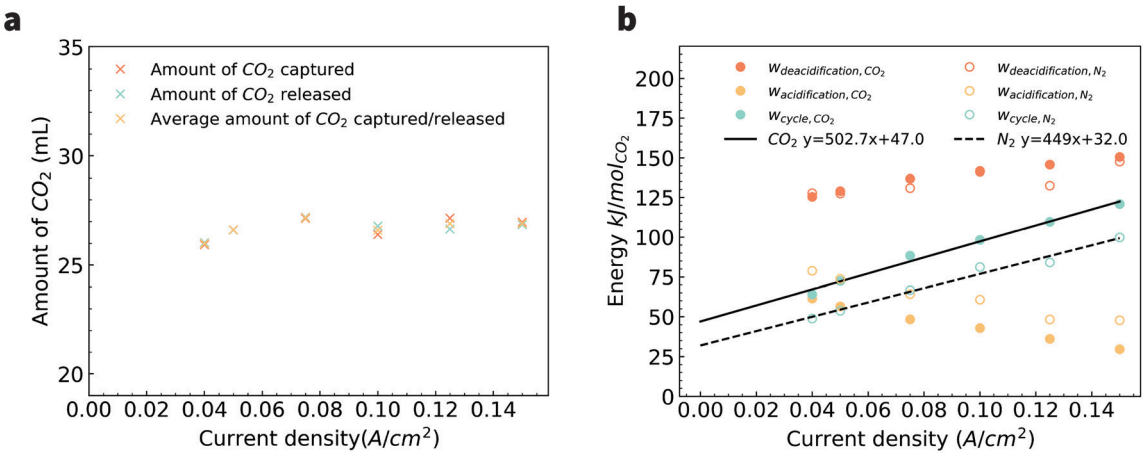

Fig. 12 (a) Average of CO_2 captured and released at different current densities. (b) Gross electrical work consumed by device ($w_{deacidification}$) during de-acidification, work returned ($w_{acidification}$) during acidification, and net work (w_{cycle}) per mole of CO_2 *vs.* current density. The work components of cycling under CO_2 and N_2 are compared.

minimum electrochemical work input for given, finite CO_2 capture/release kinetics, as the sum of the thermodynamic minimum work and the exergetic losses during the two thermodynamically irreversible processes of CO_2 release and invasion in the experimental cycle, which we call the CO_2 kinetic losses. We estimated those exergetic losses based on the average partial pressures of CO_2 in the cell headspace during CO_2 release and invasion in Fig. 11d (see ESI† Section: estimate of CO_2 kinetics losses), and obtained a value of 10.3 kJ $mol_{CO_2}^{-1}$. The gap between the estimated 10.3 kJ $mol_{CO_2}^{-1}$ and the measured 15 kJ $mol_{CO_2}^{-1}$ may be caused by uncertainties in the CO_2 kinetic loss calculation described in the ESI† (see ESI† Section: estimate of CO_2 kinetics losses) or other irreversible processes not captured by the calculation.

The predicted ideal cycle work for CO_2 separation in the four-process cycle (16–75 kJ $mol_{CO_2}^{-1}$) and the experiment-based electrical work estimate (48.9 kJ $mol_{CO_2}^{-1}$) appear competitive with other proposed methods (Table 1), particularly those in which alkaline solution is created by splitting or dissociating water.[56–61] As water splitting requires work input, theoretical minimum electrical energy inputs for CO_2 separation using these methods range between 119 and 237 kJ $mol_{CO_2}^{-1}$ (depending on pH at absorption). Because water splitting is also kinetically demanding, requiring catalysts based on precious metals such as Pt and Ru, electrical work requirements for experimentally demonstrated absorptive CO_2 capture using OH^- obtained by reactions following from water splitting are as high as 587 kJ $mol_{CO_2}^{-1}$.[60] Dissociating H_2O into H^+ and OH^- and using the latter for absorptive CO_2 capture has a lower minimum electrical energy cost, but experimentally demonstrated work inputs have been fairly high, with 405 and 300 kJ $mol_{CO_2}^{-1}$ reported in the literature.[56,61] Much lower work inputs have been reported with capture schemes in which redox reactions involving an organic[62–64] or inorganic[65] redox couple trigger capture and release of CO_2. The lowest such work inputs for complete electrochemical CO_2 capture-release cycles are 56 kJ $mol_{CO_2}^{-1}$ and 100 kJ $mol_{CO_2}^{-1}$ for capturing CO_2 *via* direct binding to a reduced quinone[64] or an electrochemically regenerated amine,[65] respectively. In the former type of cycle, CO_2 is absorbed by direct binding to a reduced quinone, followed by its release upon electrochemical oxidation; in the latter cycle, termed electrochemically mediated amine regeneration (EMAR), CO_2 binds to an amine, and is displaced upon oxidation of copper, as Cu^{2+} binds more strongly to the amine than does CO_2. In implementations of both cycles,[64,65] however, CO_2 release occurred to a partial pressure of $\sim$0 bar CO_2, which precludes direct comparison of the measured work input to a positive ideal cycle/thermodynamic minimum work input. Nevertheless, the lowest work input we obtain is 60 kJ $mol_{CO_2}^{-1}$ at 40 mA cm^{-2} (Fig. 12), which is competitive with direct binding and EMAR.[64,65]

Xie *et al.*, have demonstrated a CO_2 capture/release system using DHPS as the driver for PCET in a symmetric flow cell.[69] We refer to the oxidized form of DHPS as DHPS and the reduced form as r-DHPS. In their experiments, the catholyte and the anolyte comprised $\geq$50 mL 25 mM DHPS and r-DHPS, respectively, with saturated $NaHCO_3$ and 0.5 M Na_2SO_4 as supporting electrolyte. The feed gas in the catholyte compartment, where CO_2 absorption took place, was 15% CO_2 and 85% N_2, mimicking flue gas conditions while preventing oxidation of reduced DHPS by oxygen, and the anolyte compartment, where CO_2 was released, was filled with pure nitrogen or argon. In this setup, during the electrolysis (reducing DHPS in catholyte, oxidizing r-DHPS in anolyte), while CO_2 from the external gas source was captured by the catholyte, CO_2 from the $NaHCO_3$ was released from the anolyte. The authors reported 74 mL of CO_2 emitted from the anolyte at an energy cost of 0.492 GJ per ton (21.7 kJ $mol_{CO_2}^{-1}$) at 10 mA cm^{-2}. This value is quite close to our estimated minimum energy cost for CO_2 separation from 0.1 to 1 bar but several factors make this comparison inappropriate. One key point is that the released CO_2 was not from the captured CO_2 – a quantity that was not reported – but from previously dissolved $NaHCO_3$. Therefore, instead of showing the energy cost of a full CO_2 capture/release cycle, the energy cost presented reflected only the cost of driving 74 mL of CO_2 at 1 bar and 25 °C out of a 50 mL saturated

Table 1 Summary of thermodynamic minimum/ideal cycle and experimentally demonstrated work inputs for CO_2 separation for a variety of electrochemical and thermal methods. Where no method is specified, or the method is not specified in sufficient detail to derive minimum work for an ideal cycle, work input is the thermodynamic minimum given by the exit/inlet pressure ratio, reported in italics. Otherwise, the ideal cycle work/heat input is specified. Experimental work inputs with "th" subscript denote thermal energy inputs, whereas "e" subscript denotes electrical work input

Method	Exit/inlet pressure ratio	Thermodynamic minimum or ideal cycle (kJ $mol_{CO_2}^{-1}$)	Experimental (kJ $mol_{CO_2}^{-1}$)
	10	*5.6*	
	2500	*19*	
Fuel cell concentrator[60]	2500	119–237[a]	$469–587_e$[b]
Salt splitting[56]	N/A[c]	160[d]	405_e
Direct binding[64]	0	$-\infty$	56_e[f]
EMAR[65]	6.7	15[e]	100_e
Bipolar membrane electrodialysis[61]	2600	20[g]	$150–325_e$[h]
Quinone PCET[66]	0	$-\infty$	600_e[i]
This work	10	16–75	
	2500	30–75	
	1	0[j]	64_e[k]
	2.2	1.9[l]	$79.4–84.2_e$[m]
Traditional amine ab-/desorption[67]	8.3	*5.4*[n]	$132–150_{th}$
Shell Cansolv[11]	11.0	*5.7*[o]	103_{th}
Non-aqueous solvent amine process[10]	7.5[p]	*6.1*[q]	112[r]
Concentrated KOH[14]	375 000	31[s]	230_{th}[t]

[a] This technique captures CO_2 into an end state that is not pure gaseous CO_2. As it is based on the operation of an H_2–O_2 fuel cell, the theoretical energy input is that required to split water, which is 119 kJ $mol_{H_2O}^{-1}$ and thus 119 kJ $mol_{CO_2}^{-1}$ where CO_2 is captured as HCO_3^-, but 237 kJ $mol_{CO_2}^{-1}$ where CO_2 is captured as CO_3^{2-}. We do not consider HCO_3^- as a viable end state for capture; however it may be converted to solid carbonates in a process such as the Calera process.[68] [b] These numbers were added to the value of 350 kJ $mol_{CO_2}^{-1}$ stated in the publication in order to obtain a fair comparison value of the experimental energetic cost for DAC. [c] Exit/inlet pressure ratio is undefined because CO_2 is captured as Na_2CO_3. [d] Calculated assuming cell operates in steady-state (hydrogen oxidation reaction at pH 0, water reduction at pH 14), and that 100% of H_2 gas generated at the cathode is recovered and fed into the anode. [e] Calculated for a pressure ratio of 6.7 (15% CO_2 at the inlet, 1 atm CO_2 at the exit), including changes to open-circuit potential from CO_2 binding to amine. [f] The inlet gas source was simulated flue gas with 15% CO_2, but the outlet CO_2 partial pressure was $\sim$0 bar. Note that the energy cost was calculated based on the amount of CO_2 absorbed, and it was not clear if all the absorbed amount was released. [g] Calculated for 386 ppm CO_2 at the inlet, 1 atm CO_2 at the exit. [h] Authors assume from ref. 38 that an additional 200 kJ mol_{CO2}^{-1} would be required to operate a spray-based liquid–air contactor, however, we do not consider the contactor work input here. [i] An inlet composition with 16% CO_2 was reported, but the outlet CO_2 partial pressure was $\sim$0 bar. The experimental electrical work input was calculated for a potential of 1.0 V applied across the cell, with CO_2 captured in the form of HCO_3^- and released back to CO_2(g) with 16% mass transport efficiency (see Table 1 in ref. 66). [j] Calculated for an inlet and exit compositions of 46.5% and 46.5% CO_2, respectively, at a temperature of 20 °C. [k] Values obtained using a flow cell with 0.078 M **DSPZ** cell at 40 mA cm^{-2}. [l] Calculated for an inlet and exit compositions of 46.5% and 100% CO_2, respectively, at a temperature of 20 °C. [m] Values obtained using a flow cell with 0.09 M **DSPZ** cell at 40 mA cm^{-2}. [n] Calculated for an inlet and exit compositions of 12% and 100% CO_2, respectively, at a temperature of 35 °C. [o] Calculated for an inlet and exit compositions of 9.1% and 100% CO_2, respectively, at a temperature of 35 °C. [p] Calculated for an inlet and exit compositions of 13.3% and 100% CO_2, respectively. [q] Calculated for the system operating temperature of 90 °C. [r] The value is calculated based on the authors' claim of 33% energy saving over the aqueous amine system that has an energy consumption of 165 kJ $mol_{CO_2}^{-1}$. [s] Calculated for 400 ppm CO_2 at the inlet, 150 bar CO_2 at the exit. [t] Work input excludes electrical work required to operate air–liquid contactor, pellet reactor and auxiliary equipment.

($\geq$0.2 M) $NaHCO_3$ solution (estimated to yield $\geq$245 mL CO_2 at 1 bar when fully converted). In a similar study done by the same group, the authors demonstrated a full CO_2 capture/release cycle using riboflavin derivatives at 333 K.[70] The authors reported a low energy cost of 9.8 kJ $mol_{CO_2}^{-1}$ at a current density of 10 mA cm^{-2} but we cannot compare this number to a positive minimum work because the captured CO_2 was released at 0 bar CO_2 and their system is limited to low concentrations because of riboflavin precipitation.[70]

Watkins *et al.*,[66] demonstrated CO_2 separation from flue gas using a pH gradient created by Pt-catalyzed PCET reactions using benzoquinone and 2,6-dimethylbenzoquinone; however, the kinetic sluggishness of the associated redox reactions and the absence of an ion-selective membrane in their design result in a practical work input of 600 kJ $mol_{CO_2}^{-1}$. In contrast, the experimental cycle in our work utilized an ion-selective membrane, which allows the use of any redox-active species within a wide array of reactants capable of PCET. In the organic RFB literature, several organic molecules have been shown to have kinetic rate constants on the order of 10^{-3} cm s^{-1} or above on inexpensive carbon electrodes,[22,23,28,30,54,69,71–74] demonstrating the wide availability of reactants for CO_2 separation that will impose minimal energetic losses in an electrochemical cell.

It is worth noting that PCET-active species compatible with this CO_2 separation cycle do not have to be organic. Polyoxometalates, for instance, have attracted interest as highly soluble candidates for reactants in RFBs[75,76] and redox mediators for water splitting/reduction.[76,77] Although they tend to be insoluble and redox-inactive in basic solution,[78] they are, in principle, capable of greater than $2H^+$, $2e^-$ PCET. Chen *et al.*,[76] have demonstrated that a tungsten-based polyoxoanion can stably undergo an $18H^+$, 18 e^- redox process at a concentration of 0.5 M, with the potential to go up to 2.0 M, although its behavior in basic solution was not reported. The development of a similar reactant capable of PCET across the pH range 3–13 would effect a much larger pH swing per mole of reactant than assumed herein, thus lowering the required reactant solubility. Indeed, continued exploration of the large parameter space to which

inorganic and organic redox-active species belong may yield candidates for electrochemical CO_2 separation that boast higher redox potential, solubility and pK_a than those assumed here, and applying insights from the fields of electrocatalysis and energy storage may prove beneficial toward that goal.

In addition to minimal energetic losses, another important criterion for wide scale adoption of CO_2 separation technology is the use of low-cost cell components and working fluids. The process described here can, as shown in the experiments we performed, use water-soluble molecules and aqueous electrolytes. This is in contrast to most of the electrochemical CO_2 separation methods that do not feature the use of a pH swing which have been described in the literature, involving direct binding of CO_2 to reduced quinones[62,63,79] and oxygen-assisted conversion of CO_2 to oxalate species[80] – all of which require more expensive organic solvents or ionic liquids to operate.

DSPZ meets many requirements for an ideal molecule, including high pK_a, reasonable stability, moderate solubility and fast kinetics, but not all. **DSPZ**'s oxygen intolerance limits its application to DAC. The development of a molecule with reduction potential close to that of oxygen, as well as high solubility (>1 M) and chemical stability would make our pH swing cycle practically compatible with DAC, and we hope to stimulate the research community with this challenge.

Conclusion

In this work, we have proposed and performed a thermodynamic analysis of the energetic costs of CO_2 separation from flue gas (0.1 bar CO_2(g)) and air (400 ppm CO_2) using a pH swing created by redox reactions involving PCET. In this scheme, bulk electrolytic reduction results in the formation of alkaline solution, into which CO_2 can be absorbed, whereas oxidation of the resulting solution results in the acidification of the solution, triggering the release of pure CO_2 gas. We examined the effect of buffering from the CO_2–carbonate system on the solution pH during this pH swing, and thereby on the open-circuit potential of a hypothetical electrochemical cell in a four-process CO_2 capture-release cycle. The thermodynamic minimum work input varies from 16 to 75 kJ $mol_{CO_2}^{-1}$ as throughput increases, for both flue gas and DAC, with the potential to go substantially lower if CO_2 capture or release is performed in tandem with electrolytic reduction or oxidation. The lower limit of these values is competitive at a theoretical level with the best electrochemical CO_2 separation method we are aware of, and may result in a practical energetic cost (assuming a heat-to-work conversion efficiency of 1/3) on par with more established absorptive capture methods such as those using concentrated KOH. Additionally, its all-liquid configuration obviates the need for the precipitation and heating of solid carbonates, and compatibility with an aqueous electrolyte and potentially low-cost organic molecules implies that a CCS technology based on this concept has the potential for wide scale practical implementation. We corroborate the scheme by demonstrating CO_2 separation experiments using a **DSPZ**-based flow cell. We demonstrated one CO_2 concentrating cycle at 40 mA cm^{-2} and obtained a total cycle work of 79.4–84.2 kJ $mol_{CO_2}^{-1}$. In the low-current-density limit, we obtain an estimated total cycle work of 48.9 kJ $mol_{CO_2}^{-1}$ for absorbing CO_2 from a 0.465 bar CO_2 source and releasing to a 1.0 bar CO_2 stream. The experimental cycle work in the low-current-density limit is comparable to the value of 34 kJ $mol_{CO_2}^{-1}$ for CO_2 separation predicted by our thermodynamic analysis for these conditions. This relatively small difference, compared to other methods summarized in Table 1, is encouraging. To best of our knowledge, this is the first demonstrated stable, reversible, multi-cycle electrochemical CCS device utilizing a flow cell framework. These promising results shed light on future low energy electrochemical CCS devices using our proposed scheme.

Conflicts of interest

There are no conflicts of interest to declare.

Acknowledgements

This research was supported by a grant from the Harvard University Climate Change Solutions Fund. We thank Daniel Schrag, Daniel Nocera, David Keith, Steven Wofsy, Robert Gustafson, Andrew Wong, Eric Fell, Toly Rinberg and Andrew Bergman for helpful discussions.

References

1 M. R. Raupach, G. Marland, P. Ciais, C. Le Quere, J. G. Canadell, G. Klepper and C. B. Field, *Proc. Natl. Acad. Sci. U. S. A.*, 2007, **104**, 10288–10293.
2 S. Pacala and R. Socolow, *Science*, 2004, **305**, 968–971.
3 IPCC, Climate Change 2014: Synthesis Report, IPCC, Geneva, Switzerland, 2014.
4 K. Z. House, C. F. Harvey, M. J. Aziz and D. P. Schrag, *Energy Environ. Sci.*, 2009, **2**, 193.
5 K. S. Lackner, S. Brennan, J. M. Matter, A. H. Park, A. Wright and B. van der Zwaan, *Proc. Natl. Acad. Sci. U. S. A.*, 2012, **109**, 13156–13162.
6 K. Z. House, A. C. Baclig, M. Ranjan, E. A. van Nierop, J. Wilcox and H. J. Herzog, *Proc. Natl. Acad. Sci. U. S. A.*, 2011, **108**, 20428–20433.
7 Y. Yuan and G. T. Rochelle, *Int. J. Greenhouse Gas Control*, 2019, **84**, 82–90.
8 F. Vega, F. M. Baena-Moreno, L. M. G. Fernández, E. Portillo and B. Navarrete, *Appl. Energy*, 2020, **260**, 114313.
9 D. J. Heldebrant, P. K. Koech, V.-A. Glezakou, R. Rousseau, D. Malhotra and D. C. Cantu, *Chem. Rev.*, 2017, **117**, 9594–9624.
10 M. Lail, J. Tanthana and L. Coleman, *Energy Procedia*, 2014, **63**, 580–594.
11 A. Singh and K. Stéphenne, *Energy Procedia*, 2014, **63**, 1678–1685.
12 P. H. M. Feron, A. Cousins, K. Jiang, R. Zhai and M. Garcia, *Fuel*, 2020, **273**, 117776.

13 M. Mahmoudkhani and D. W. Keith, *Int. J. Greenhouse Gas Control*, 2009, **3**, 376–384.
14 D. W. Keith, G. Holmes, D. St. Angelo and K. Heidel, *Joule*, 2018, **2**, 1573–1594.
15 D. G. Kwabi and M. Aziz, *Chemrxiv*, 2019, DOI: 10.26434/chemrxiv.7853414.
16 C. Costentin, *Chem. Rev.*, 2008, **108**, 2145–2179.
17 E. Laviron, *J. Electroanal. Chem.*, 1984, **169**, 29–46.
18 M. Quan, D. Sanchez, M. F. Wasylkiw and D. K. Smith, *J Am. Chem. Soc.*, 2007, **129**, 12847–12856.
19 M. Rahimi, G. Catalini, S. Hariharan, M. Wang, M. Puccini and T. A. Hatton, *Cell Rep. Phys. Sci.*, 2020, **1**(4), 100033.
20 M. Rahimi, G. Catalini, M. Puccini and T. A. Hatton, *RSC Adv.*, 2020, **10**, 16832–16843.
21 M. H. V. Huynh and T. J. Meyer, *Chem. Rev.*, 2007, **107**, 5004–5064.
22 B. T. Huskinson, M. P. Marshak, C. Suh, S. Er, M. R. Gerhardt, C. J. Galvin, X. Chen, A. Aspuru-Guzik, R. G. Gordon and M. J. Aziz, *Nature*, 2014, **505**, 195–198.
23 K. Lin, Q. Chen, M. R. Gerhardt, L. Tong, S. B. Kim, L. Eisenach, A. W. Valle, D. Hardee, R. G. Gordon, M. J. Aziz and M. P. Marshak, *Science*, 2015, **349**, 1529.
24 K. Lin, R. Gómez-Bombarelli, E. S. Beh, L. Tong, Q. Chen, A. Valle, A. Aspuru-Guzik, M. J. Aziz and R. G. Gordon, *Nat. Energy*, 2016, **1**, 16102.
25 B. Yang, L. Hoober-Burkhardt, S. Krishnamoorthy, A. Murali, G. K. S. Prakash and S. R. Narayanan, *J. Electrochem. Soc.*, 2016, **163**, A1442–A1449.
26 D. G. Kwabi, K. Lin, Y. Ji, E. F. Kerr, M.-A. Goulet, D. DePorcellinis, D. P. Tabor, D. A. Pollack, A. Aspuru-Guzik, R. G. Gordon and M. J. Aziz, *Joule*, 2018, **2**, 1907.
27 Y. Ji, M. A. Goulet, D. A. Pollack, D. G. Kwabi, S. Jin, D. Porcellinis, E. F. Kerr, R. G. Gordon and M. J. Aziz, *Adv. Energy Mater.*, 2019, **9**, 1900039.
28 S. Jin, Y. Jing, D. G. Kwabi, Y. Ji, L. Tong, D. De Porcellinis, M. A. Goulet, D. A. Pollack, R. G. Gordon and M. J. Aziz, *ACS Energy Lett.*, 2019, **4**, 1342–1348.
29 L. Tong, M.-A. Goulet, D. P. Tabor, E. F. Kerr, D. De Porcellinis, E. M. Fell, A. Aspuru-Guzik, R. G. Gordon and M. J. Aziz, *ACS Energy Lett.*, 2019, **4**, 1880–1887.
30 W. Min, J. Yan, A. A. Wong, E. M. Fell, J. Shijian, T. Zhijiang, G. Roy and M. J. Aziz, *Chem*, 2020, **6**(6), 1432–1442.
31 D. G. Kwabi, Y. Ji and M. J. Aziz, *Chem. Rev.*, 2020, **120**(14), 6467–6489.
32 L. Hoober-Burkhardt, S. Krishnamoorthy, B. Yang, A. Murali, A. Nirmalchandar, G. K. Surya Prakash and S. R. Narayanan, *J. Electrochem. Soc.*, 2017, **164**, A600–A607.
33 J. D. Milshtein, L. Su, C. Liou, A. F. Badel and F. R. Brushett, *Electrochim. Acta*, 2015, **180**, 695–704.
34 C. Wang, X. Li, B. Yu, Y. Wang, Z. Yang, H. Wang, H. Lin, J. Ma, G. Li and Z. Jin, *ACS Energy Lett.*, 2020, **5**, 411–417.
35 A. Hollas, X. Wei, V. Murugesan, Z. Nie, B. Li, D. Reed, J. Liu, V. Sprenkle and W. Wang, *Nat. Energy*, 2018, **3**, 508–514.
36 R. E. Zeebe and D. Wolf-Gladrow, *CO2 in Seawater: Equilibrium, Kinetics, Isotopes*, Elsevier, Amsterdam, 2005.
37 R. N. Roy, L. N. Roy, K. M. Vogel, C. Porter-Moore, T. Pearson, C. E. Good, F. J. Millero and D. M. Campbell, *Mar. Chem.*, 1993, **44**, 249–267.
38 J. K. Stolaroff, D. W. Keith and G. V. Lowry, *Environ. Sci. Technol.*, 2008, **42**, 2728–2735.
39 K. G. Schulz, U. Riebesell, B. Rost, S. Thoms and R. E. Zeebe, *Mar. Chem.*, 2006, **100**, 53–65.
40 J. da Costa Ores, L. Sala, G. P. Cerveira and S. J. Kalil, *Chemosphere*, 2012, **88**, 255–259.
41 M. A. Henderson, D. W. Keith, A. P. S. Kainth, K. R. HEIDEL and J. A. Ritchie, *US Pat.*, 8,871,008 B2, 2014.
42 I. M. Power, A. L. Harrison, G. M. Dipple and G. Southam, *Int. J. Greenhouse Gas Control*, 2013, **16**, 145–155.
43 S. Kim, J. Chen, T. Cheng, A. Gindulyte, J. He, S. He, Q. Li, B. A. Shoemaker, P. A. Thiessen, B. Yu, L. Zaslavsky, J. Zhang and E. E. Bolton, *Nucleic Acids Res.*, 2019, **47**, D1102–D1109.
44 H. Schultz, G. Bauer, E. Schachl, F. Hagedorn and P. Schmittinger, *Ullmann's Encyclopedia of Industrial Chemistry*, Wiley-VCH, Weinheim, 2000, vol. 29, p. 701.
45 A. A. Wong, M. J. Aziz and S. M. Rubinstein, presented in part at the 231st ECS Meeting, New Orleans, LA, May 28 – June 1, 2017, 2017.
46 M. D. R. Kok and J. T. Gostick, *J. Membr. Sci.*, 2015, **473**, 237–244.
47 M. R. Gerhardt, A. A. Wong and M. J. Aziz, *J. Electrochem. Soc.*, 2018, **165**, A2625–A2643.
48 T. Lopes, M. Ho, B. K. Kakati and A. R. J. Kucernak, *J. Power Sources*, 2015, **274**, 382–392.
49 C. Yin, Y. Gao, S. Guo and H. Tang, *Energy*, 2014, **74**, 886–895.
50 X. Ke, J. M. Prahl, J. I. D. Alexander and R. F. Savinell, *J. Power Sources*, 2018, **384**, 295–302.
51 M. Messaggi, P. Canzi, R. Mereu, A. Baricci, F. Inzoli, A. Casalegno and M. Zago, *Appl. Energy*, 2018, **228**, 1057–1070.
52 G. Holmes and D. W. Keith, *Philos. Trans. R. Soc., A*, 2012, **370**, 4380–4403.
53 D. Desai, E. S. Beh, S. Sahu, V. Vedharathinam, Q. van Overmeere, C. F. de Lannoy, A. P. Jose, A. R. Völkel and J. B. Rivest, *ACS Energy Lett.*, 2018, **3**, 375–379.
54 Q. Chen, M. R. Gerhardt and M. J. Aziz, *J. Electrochem. Soc.*, 2017, **164**, A1126–A1132.
55 S. Kaerer, C. Rakousky, J. Melke and C. Roth, *J. Appl. Electrochem.*, 2013, **43**, 1069–1078.
56 A. Mehmood, M. I. Iqbal, J.-Y. Lee, J. Hwang, K.-D. Jung and H. Y. Ha, *Electrochim. Acta*, 2016, **219**, 655–663.
57 R. J. Gilliam, B. K. Boggs, V. Decker, M. A. Kostowskyj, S. Gorer, T. A. Albrecht, J. D. Way, D. W. Kirk and A. J. Bard, *J. Electrochem. Soc.*, 2012, **159**, B627–B628.
58 G. H. Rau, *Energy Procedia*, 2009, **1**, 823–828.
59 S. Datta, M. P. Henry, Y. J. Lin, A. T. Fracaro, C. S. Millard, S. W. Snyder, R. L. Stiles, J. Shah, J. Yuan, L. Wesoloski, R. W. Dorner and W. M. Carlson, *Ind. Eng. Chem. Res.*, 2013, **52**, 15177–15186.
60 M. Eisaman, D. Schwartz, S. Amic, D. Larner, J. Zesch, F. Torres and K. Littau, 2009.
61 M. D. Eisaman, L. Alvarado, D. Larner, P. Wang, B. Garg and K. A. Littau, *Energy Environ. Sci.*, 2011, **4**, 1319–1328.

62 B. Gurkan, F. Simeon and T. A. Hatton, *ACS Sustainable Chem. Eng.*, 2015, **3**, 1394–1405.
63 S. Voskian and T. A. Hatton, *Energy Environ. Sci.*, 2019, **12**, 3530–3547.
64 Y. Liu, H.-Z. Ye, K. M. Diederichsen, T. V. Voorhis and T. A. Hatton, *Nat. Commun.*, 2020, **11**, 2278.
65 M. C. Stern, F. Simeon, H. Herzog and T. A. Hatton, *Energy Environ. Sci.*, 2013, **6**, 2505–2517.
66 J. D. Watkins, N. S. Siefert, X. Zhou, C. R. Myers, J. R. Kitchin, D. P. Hopkinson and H. B. Nulwala, *Energy Fuels*, 2015, **29**, 7508–7515.
67 K. Goto, S. Kodama, T. Higashii and H. Kitamura, *J. Chem. Eng. Jpn.*, 2014, **47**, 663–665.
68 B. R. Constantz, P. Valley, A. Youngs, P. B. Tuet, S. Omelon, K. Farsad, S. Jose, R. J. Gilliam, V. Decker, D. W. Kirk, J. D. Way, A. J. Bard, R. Danziger, M. Fernandez and C. Ryan, *US Pat.*, 7,887,694 B2, 2011.
69 H. Xie, Y. Wu, T. Liu, F. Wang, B. Chen and B. Liang, *Appl. Energy*, 2020, **259**, 114119.
70 H. Xie, W. Jiang, T. Liu, Y. Wu, Y. Wang, B. Chen, D. Niu and B. Liang, *Cell Rep. Phys. Sci.*, 2020, **1**, 100046.
71 C. DeBruler, H. Bo, M. Jared, L. Jian and T. Leo Liu, *ACS Energy Lett.*, 2018, **3**, 663–668.
72 E. S. Beh, D. De Porcellinis, R. L. Gracia, K. T. Xia, R. G. Gordon and M. J. Aziz, *ACS Energy Lett.*, 2017, **2**, 639–644.
73 J. L. Barton, J. D. Milshtein, J. J. Hinricher and F. R. Brushett, *J. Power Sources*, 2018, **399**, 133–143.
74 S. Jin, E. M. Fell, L. Vina-Lopez, Y. Jing, P. W. Michalak, R. G. Gordon and M. J. Aziz, *Adv. Energy Mater.*, 2020, **10**, 2000100.
75 H. D. Pratt, N. S. Hudak, X. Fang and T. M. Anderson, *J. Power Sources*, 2013, **236**, 259–264.
76 J. J. Chen, M. D. Symes and L. Cronin, *Nat. Chem.*, 2018, **10**, 1042–1047.
77 B. Rausch, M. D. Symes, G. Chisholm and L. Cronin, *Science*, 2014, **345**, 1326–1330.
78 C. V. Krishnan, M. Garnett, B. Hsiao and B. Chu, *Int. J. Electrochem. Sci.*, 2007, **2**, 29–51.
79 P. Scovazzo, J. Poshusta, D. DuBois, C. Koval and R. Noble, *J. Electrochem. Soc.*, 2003, **150**, D91.
80 W. I. Al Sadat and L. Archer, *Sci. Adv.*, 2016, **2**, 1–10.

Electronic Supplementary Information

for

pH Swing Cycle for CO_2 Capture Electrochemically Driven through Proton-Coupled Electron Transfer

Shijian Jin[†], Min Wu[†], Roy Gordon[‡], Michael J. Aziz[†*] and David G. Kwabi[†§]

[†] John A. Paulson School of Engineering and Applied Sciences, Harvard University, Cambridge, Massachusetts, 02138, United States

[‡]Department of Chemistry and Chemical Biology, Harvard University, Cambridge, Massachusetts 02138, United States

*maziz [at] harvard [dot] edu
[§]Present address: Department of Mechanical Engineering, University of Michigan, Ann Arbor MI 48109 USA. dkwabi [at] umich [dot] edu

Table of Figures

Table of Sections

Table of Tables

Table S1. Table of acronyms

Acronyms	Explanation
AEM	anion exchange membrane
AHP	2-amino-3-hydroxyphenazine
BHPC	benzo[a]hydroxyphenazine-7/8-carboxylic acid
CCS	carbon capture and sequestration
CEM	cation exchange membrane
DAC	direct air capture
DHPS	Phenazine dihydroxysulfonic acid
DIC	dissolved inorganic carbon
DSPZ	sodium 3,3'-(phenazine-2,3-diylbis(oxy))bis(propane-1-sulfonate)
EMAR	electrochemically mediated amine regeneration
HP	2-hydroxyphenazine
MEA	monoethanolamine
PCET	proton-coupled electron transfer
RFB	redox-flow batteries
TA	total alkalinity

Thermodynamic Analysis

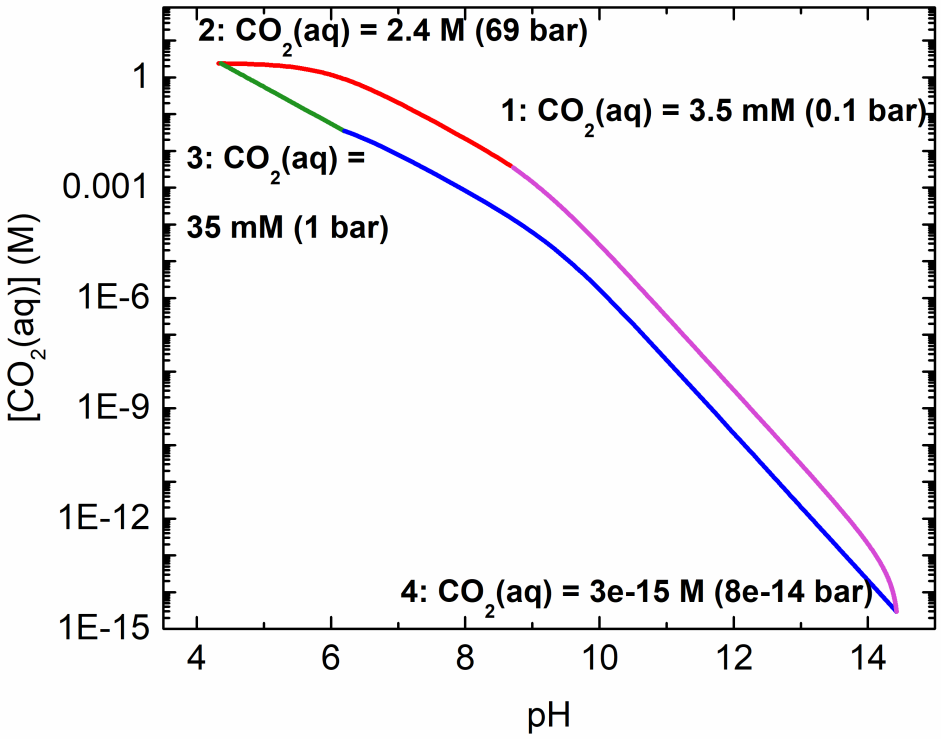

Figure S1. CO_2(aq) vs. pH during the 4-process cycle described in **Figure 4**. Processes 1→2 and 2→3 are depicted with red lines, and processes 3→4 and 4→1 are depicted in blue lines. The equilibrium CO_2 pressure corresponding to each CO_2(aq) is stated.

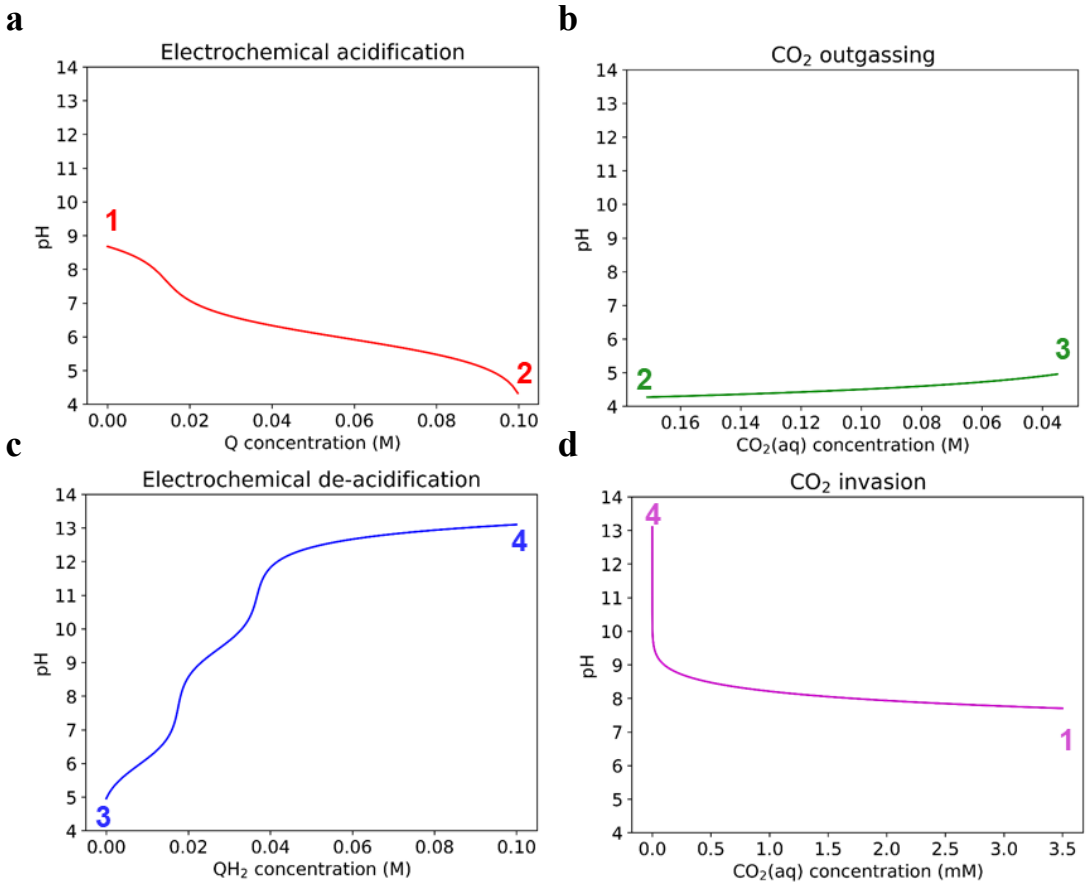

Figure S2. Ideal CO_2 separation cycle for starting *QH_2* concentration of 0.1 M, DIC concentration of 0.175 M and an exit/inlet pressure ratio of 10, which translates to an outgassing overpressure of 5. pH as a function of Q and QH_2 concentration and CO_2(aq) during (a) electrochemical acidification (process 1 → 2) (b) CO_2 outgassing (process 2 → 3) (c) electrochemical de-acidification (process 3 → 4) and (d) CO_2 invasion (process 4 → 1), at the end of which aqueous CO_2 (CO_2(aq)) is assumed to be in equilibrium with 0.1 bar CO_2 gas.

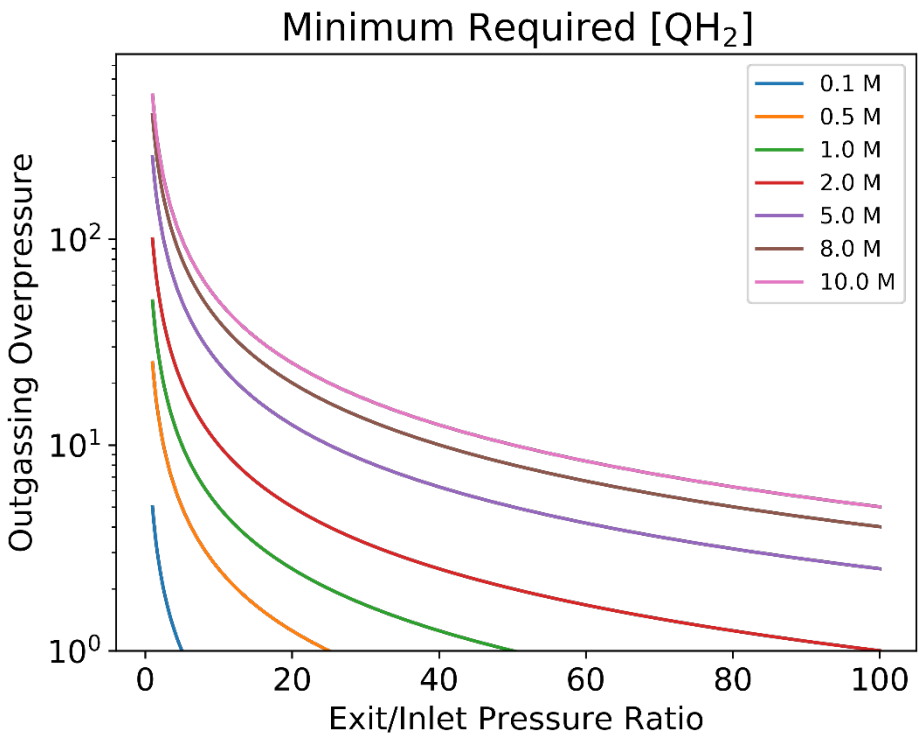

Figure S3. Relationship between outgassing overpressure and exit/inlet pressure ratio for various [QH_2] values at State 1 between 0.1 and 8.0 M, assuming the solution at State 1 is in equilibrium with 0.1 bar CO_2 gas.

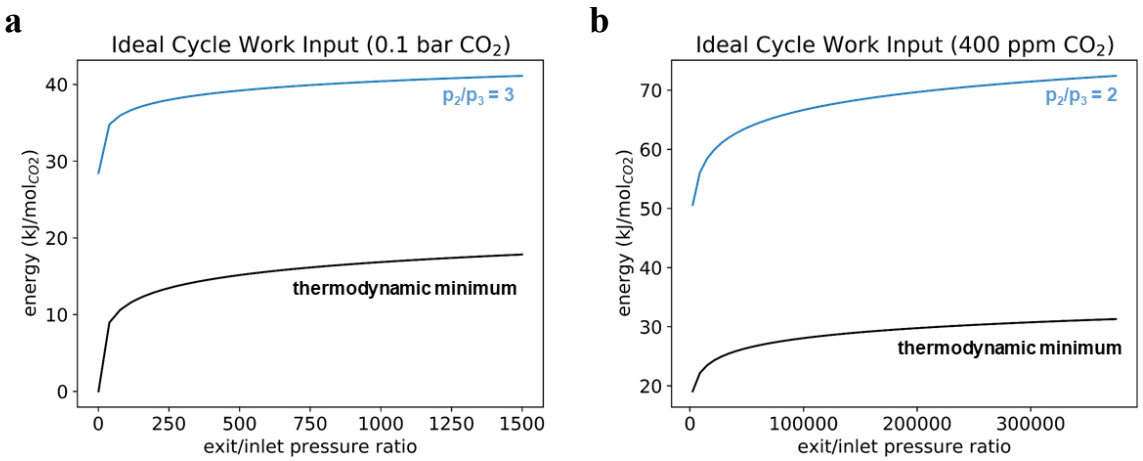

Figure S4. Ideal cycle work vs exit/inlet pressure ratios for inlet streams at (a) 0.1 bar and (b) 400 ppm CO_2. The highest exit/inlet pressure ratio represents an exit pressure of 150 bar CO_2(g), and the maximum overpressure plotted in each case is based on the assumption that QH_2 concentration can reach up to 10 M.

1 *Estimation of Final pH after Electrochemical De-acidification.*

The relative concentration of protonated/deprotonated reduced Q is given by the Henderson-Hasselbalch equation, which relates solution pH to the pKa of QH_2 and the concentrations:

$$pH = pK_a + log_{10}\frac{[Q^{2-}]}{[QH_2]}. \textit{ eq. S 1}$$

By assuming that each mole of QH_2 created by the bulk electrolytic reduction of a mole of Q removes 2 moles of H^+ from solution, we can calculate the final pH of a given solution given its initial pH, the concentration of Q, and the pK_a of Q. The final pH is given by:

$$pH = 14 - pOH, \textit{ eq. S 2}$$

where *p*OH is defined based on the logarithmic constant for OH^- concentration, as $-\log_{10}[OH^-]$. Because the final pH is the sum of the initial OH^- concentration and OH^- ions created by electrochemical reduction of Q, we may re-write the above equation as:

$$pH = 14 + log_{10}(OH_0^- + OH_n^-), \textit{ eq. S 3}$$

where OH_0^- is the initial OH^- concentration and OH_n^- represents newly created OH^-. Based on the Henderson-Hasselbalch equation, one can re-express solution pH as a function of starting reactant concentration Q and its protonated reduced form, QH_2:

$$10^{(pH-pK_a)} = \frac{[Q^{2-}]}{[QH_2]} = \frac{[Q-QH_2]}{[QH_2]} = \frac{[Q]}{[QH_2]} - 1. \textit{ eq. S 4}$$

By re-arranging terms and assuming that the formation of each new QH_2 produces two OH^- ions, we obtain an expression for OH_n^-:

$$OH_n^- = \frac{2Q}{1+10^{(pH-pKa)}}. \textit{ eq. S 5}$$

Plugging this expression for OH_n^- into eq. S1 provides the full relationship between solution pH, pK_a, initial pH and Q concentration:

$$pH = 14 + log_{10}\left(10^{(pH_0-14)} + \frac{2Q}{1+10^{(pH-pKa)}}\right). \textit{ eq. S 6}$$

The plot below depicts final pH upon full reduction of Q as a function of pKa for a solution with initial pH 3 and a series of Q concentrations ranging from 50 mM to 2.0 M.

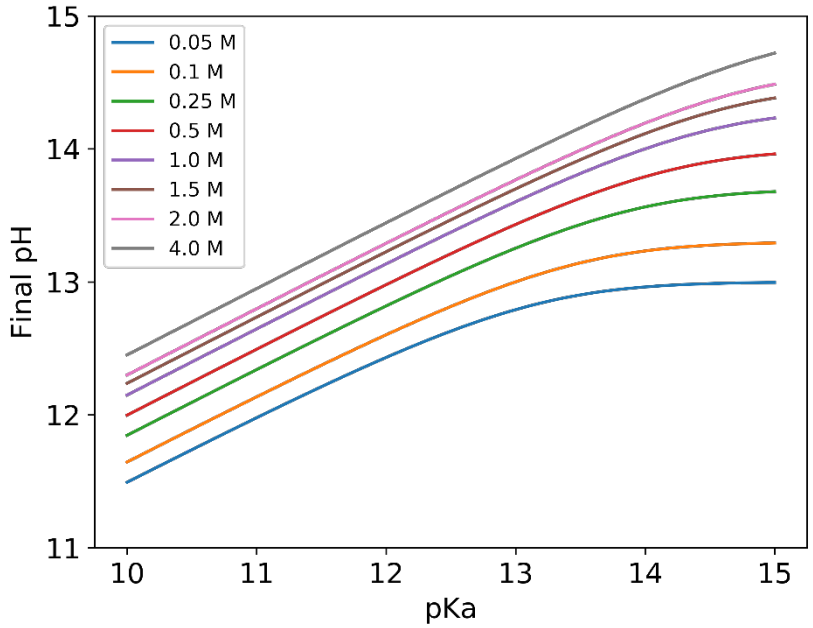

Figure S5. Relationship between pKa of *Q* and final pH upon reduction of *Q* based on the solution to implicit equation S6 for a series of *Q* concentrations between 50 mM and 2.0 M.

It is important to note two assumptions that have been made: (1) the solution is completely unbuffered; and (2) *Q* has one pKa at which protons are in equilibrium with its deprotonated reduced form. As has been shown in the RFB literature, this is the case for some redox-active species (such as 2,6-dihydroxyanthraquinone [1]) but is not generally true for all reactants capable of PCET, which may have two distinct pKa values for each proton.[2] The main consequence of these assumptions is that the final pH computed above represents an upper limit, as buffering effects will reduce the power of PCET to effect pH shifts, and the presence two distinct pKa values imply a regime in which two-electron reduction will be accompanied by removal of one rather than two protons from solution.

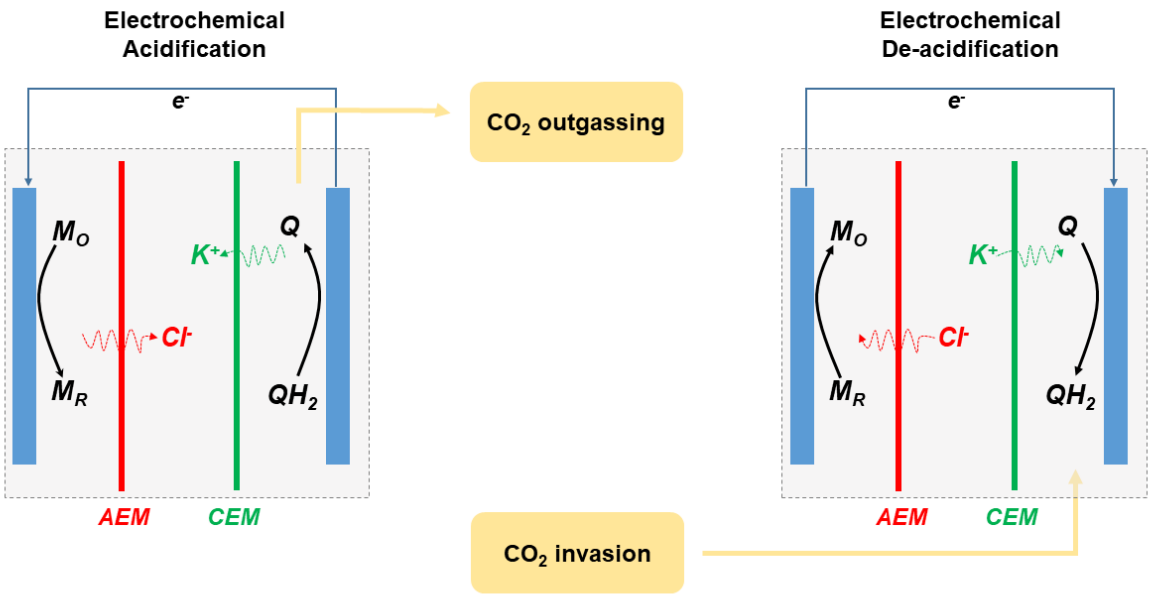

Figure S6. Schematic of two-membrane electrochemical cell, showing how electrochemical acidification and de-acidification processes are integrated with CO_2 outgassing and invasion. A KCl supporting salt is assumed, and K^+ and Cl^- ions move through the CEM and AEM, respectively, to/from a middle electrolyte chamber. M_O and M_R, represent the redox processes occurring counter to Q/QH_2, and could be either symmetric (i.e. QH_2/Q) or asymmetric (i.e. employing some other redox couple), the latter case implying that CCS could be integrated with energy storage.

Experimental

2 Synthesis and Characterization

All chemicals were purchased from Sigma-Aldrich or Acros Organics unless specified otherwise. All chemicals were used as received unless specified otherwise.

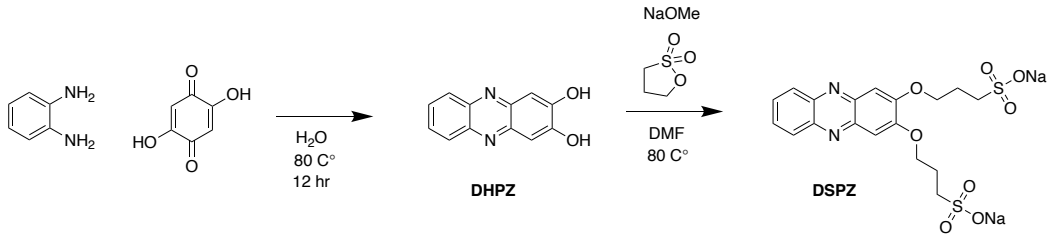

Scheme S1. Synthesis of 1,1'-bis(3-phosphonopropyl)-[4,4'-bipyridine]-1,1'-diium dibromide (DSPZ)

benzene-1,2-diamine (1 equiv.) was mixed with 2,5-dihydroxycyclohexa-2,5-diene-1,4-dione (1.03 equiv.) in water to achieve 0.2 M benzene-1,2-diamine solution in a pressure vessel. The reaction mixture was refluxed at 80 °C and stirred overnight. The resulting slurry was filtered and the black precipitate was crude product phenazine-2,3-diol (DHPZ). The black precipitate was then dissolved in 0.1 M KOH solution to make a 0.02 M DHPZ solution. The solution was filtered again and the filtrate was acidified with HCl solution until pH 7. Red precipitates formed and were filtered to give pure DHPZ (99% yield).

DHPZ (1 equiv.) was dissolved in DMF to make 0.1 M DHPZ solution. A methanoal solution of sodium methoxide (3 equiv. NaOMe) was added to the DHPZ solution under N_2. 2.5 equiv. propane sultone was then added into the solution. The reaction mixture was stirred overnight at 80 °C to give an red slurry. The slurry was then cooled and filtered. The red precipitates were washed thoroughly with ethyl acetate to remove residual DMF. The final DSPZ products were red solids (88% yield)

DSPZ: ^{1}H NMR (500 MHz, D_2O) δ 7.40-7.48 (m, 2H), 7.22-7.27 (m, 2H), 5.84 (s, 2H), 3.65-3.75 (m, 4H) , 3.03-3.09 (m, 4H), 2.12-2.22 (m, 4H),

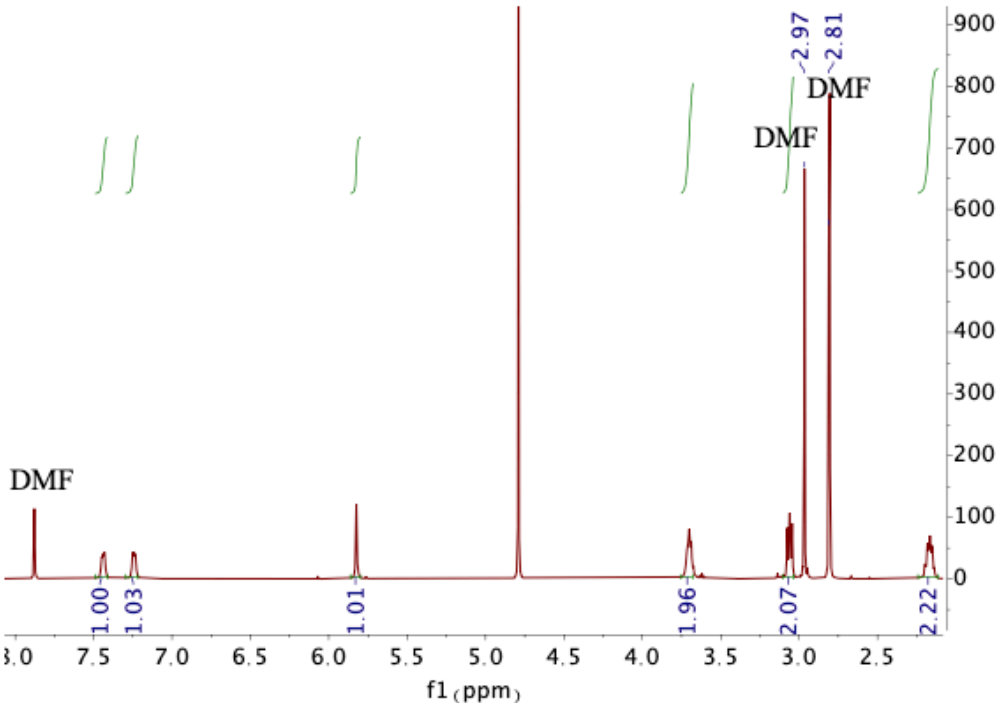

Figure S7. 1H NMR spectrum of DSPZ in DMSO-d6. The solvent DMF remained in the solution.

The solubility of DSPZ was measured using UV-Vis spectroscopy. A calibration line was obtained using the absorption peak at 395 nm of 10, 20, 40 and 50 μM DSPZ solutions. An aliquot of saturated DSPZ solution (in 1 M KCl or KOH, with 1 vol% anti-foam agent) was diluted 20,000 times, and then the absorption spectrum of the diluted solution was measured. The calculated solubility values for DSPZ in 1 M KCl (pH = 5.9) and in 1 M KOH (pH =14) are both 0.73 M. **Figure S8** shows the calibration line and the absorbance of the 20,000 times diluted saturated solution.

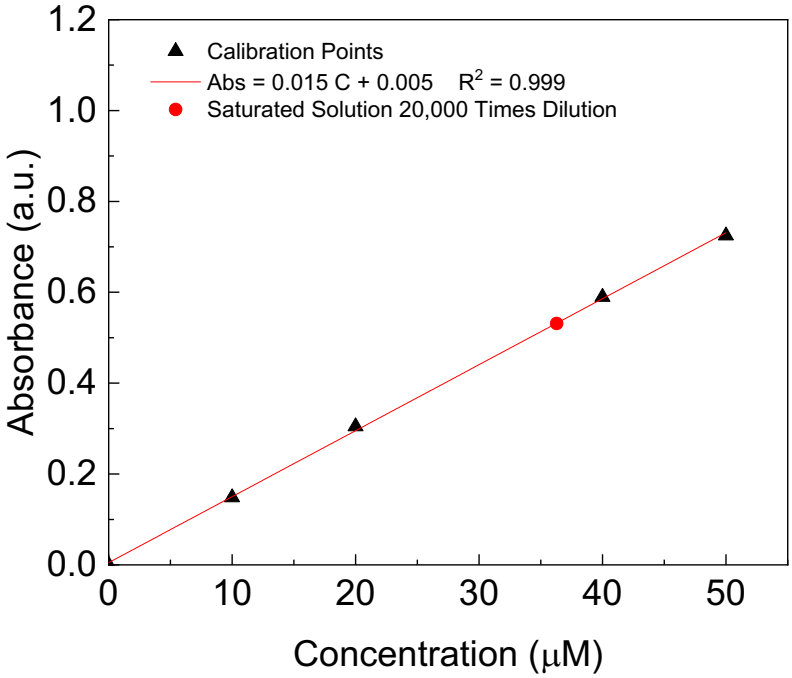

Figure S8. Calibration line and the measured solubility (0.73 M at pH 6.8 and 14) of DSPZ.

3 *Electrochemistry*

Glassy carbon (BASi MF-2012, 3.0mm diameter) was used as the working electrode for all three-electrode CV tests. A Ag/AgCl reference electrode (BASi MF-2052, pre-soaked in 3 M NaCl solution), and a graphite counter electrode were used for CV tests. CV tests and cell cycling were performed using a Gamry Reference 3000 potentiostat. 0.1 mL of antifoam B emulsion purchased from Sigma-Aldrich was added into the negolyte solution before cell cycling in order to prevent foam formation.

Flow cell experiments were constructed with cell hardware from Fuel Cell Tech. (Albuquerque, NM), assembled into a zero-gap flow cell configuration, similar to a previous report.[1] Pyrosealed POCO graphite flow plates with serpentine flow patterns were used for both electrodes. Each electrode comprised a 5 cm^2 geometric surface area covered by a stack of four sheets of Sigracet SGL 39AA porous carbon paper pre-baked in air for 24 h at 400 °C. The specific area of SGL 39AA carbon paper is 0.5 m^2/g, as reported by Forner-Cuenca *et al.*[3] The outer portion of the space between the electrodes was gasketed by Viton sheets with the area over the electrodes cut out. Torque applied during cell assembly was 60 lb-in on each of 8 bolts. Posolytes were fed into the cell through fluorinated ethylene propylene (FEP) tubing at a rate of 100 mL/min controlled by a Cole-Parmer 6 Masterflex L/S peristaltic pump, and the negolytes were circulated at the same rate controlled by a Cole-Parmer Masterflex digital benchtop gear pump system. The flowmeter used in the gas outlet was a Honeywell AWM3150V. The CO_2 sensor was an ExplorIR-W 100% CO_2 sensor purchased from co2meter.com. Gases exited the negolyte chamber and reached the CO_2 sensor via a 10 cm FEP tubing with 1/16'' ID. As shown in **Figure 9**, a drierite drying tube (Cole Parmer) and the flowmeter were in between the CO_2 sensor and the negolyte chamber, along the

gas path. It took ~220 seconds for the gases at 10 mL/min to reach the CO_2 sensor from the negolyte chamber.

4 CO_2 Capture from 0.465 bar and Release to 1 bar

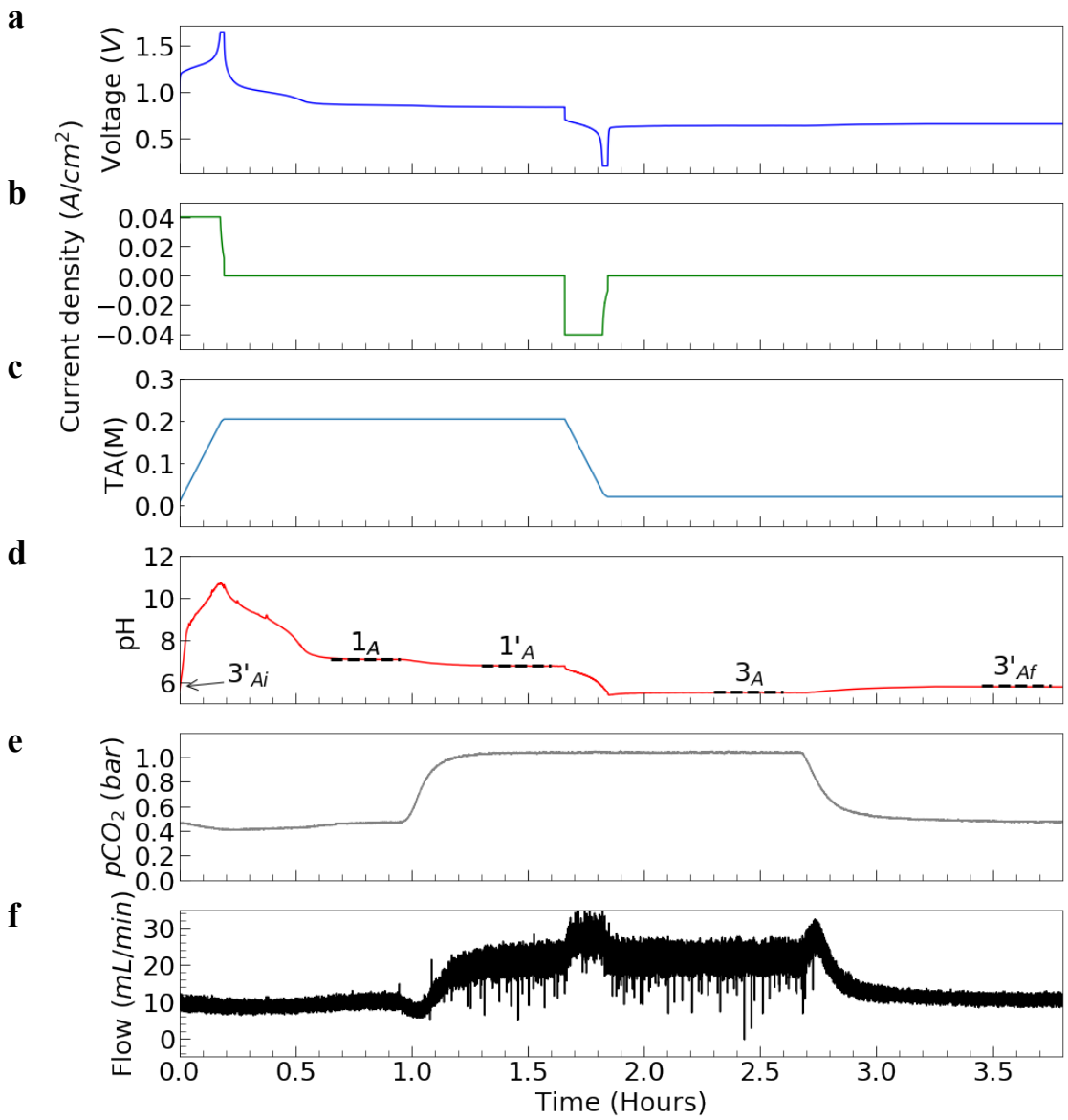

Figure S9 The concentrating cycle **A.** One full CO_2 capture/release cycle with 0.465/1 bar inlet/exit pressure using a DSPZ based flow cell at 40 mA/cm^2. Electrolytes comprised 7 mL 0.09 M DSPZ in 1 M KCl (negolyte, capacity limiting side, theoretical capacity = 121.6 C) and 40 mL of 0.1 M $K_4Fe(CN)_6$ and 0.1 M $K_3Fe(CN)_6$ in 1 M KCl (posolyte, non-capacity limiting side) (a) Voltage profile. (b) Current density. (c) Estimated total alkalinity. (d) pH. States 3'$_{Ai}$, 1$_A$, 1'$_A$, 3$_A$ and 3'$_{Af}$ represent pH values before deacidification under 0.465 bar pCO_2, after deacidification/absorption under 0.465 bar pCO_2, after changing pCO_2 from 0.465 bar to 1 bar, after acidification/desorption under 1 bar and after changing pCO_2 from 1 bar to 0.465 bar,

respectively. (e) CO_2 partial pressure. (f) Total gas flow rate. Note that the gas flow rate undergoes large fluctuations between 1.2 and 2.6 hour.

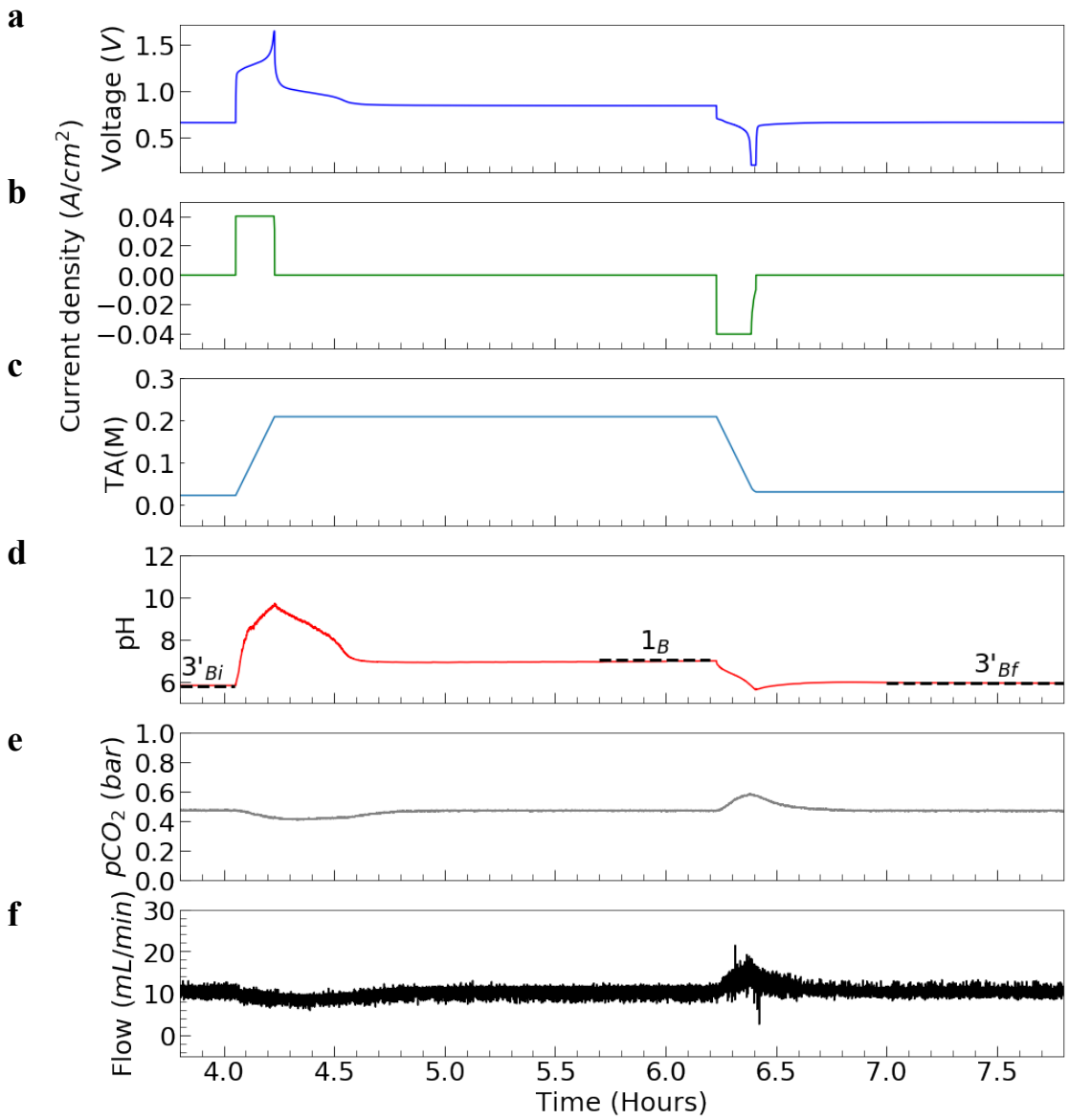

Figure S10. The non-concentrating cycle B. One full CO_2 capture/release cycle with 0.465/0.465 bar inlet/exit pressure using the same cell as in **Figure S9**. (a) Voltage profile. (b) Current density. (c) Estimated total alkalinity. (d) pH. $3'_{Bi}$, 1_B, and $3'_{Bf}$ represent pH values before deacidification under 0.465 bar pCO_2, after deacidification/absorption under 0.465 bar pCO_2 , and after acidification/desorption under 0.465 bar pCO_2, respectively. (e) CO_2 partial pressure. (f) Total gas flow rate.

Figure S9 demonstrates a CO_2 separation cycle where deacidification/CO_2 invasion take place at pCO_2 = 0.465 bar and acidification/CO_2 release take place at pCO_2 = 1 bar. **Figure S10** shows a subsequent cycle where both deacidification/CO_2 invasion and acidification/CO_2 release take place at pCO_2 = 0.465 bar. We refer to the former cycle as concentrating cycle A and the latter cycle as non-concentrating cycle B. In concentrating cycle A, we adjusted the nominal pCO_2 from

0.465 to 1 bar at the end of CO_2 invasion about ~ 55 minutes after the start of the experiment (**Figure S9)**. This adjustment took about 20 minutes to complete and resulted in large fluctuations in gas flow rate (**Figure S9f,** 0.9 - 1.2 hour). Similarly long transient behavior took place again at the end of CO_2 release when we adjusted pCO_2 back to 0.465 bar (**Figure S9**e and f**,** 2.7 - 3.0 hour). These large fluctuations and long transients make the calculation of CO_2 absorbed or released via eq. 13 difficult. Therefore, for both cycles, we estimated DIC values using pH values at states $3'_{Ai}$ to $3'_{Af}$ (**Figure S9**d), TA and eq. 5-10. Note that states 3_A and 1_A in concentrating cycle A correspond to states 3 and 1 in **Figure 5** and **Figure 6**, except for higher pCO_2 and lower concentration of redox-active molecules. States $3'_A$ and $1'_A$ are similar to the corners part way through the two-stage acidification and two-stage deacidification processes in **Figure 5** and **Figure 6**. The difference is that DIC is kept constant from states 3 or 1 to the corners in **Figure 5** and **Figure 6**, whereas TA is kept constant from states $3_A/1_A$ to $3'_A/1'_A$ in the concentrating cycle A. Due to possible side reactions and/or inaccuracy in pH measurement, the initial $3'_A$ and final $3'_A$ states have slightly different pH values. Therefore, we add the subscripts "i" and "f" to denote the initial and final $3'_A$ states. The same nomenclature applies to the states in non-concentrating cycle B. We estimated DIC values under either of two assumptions. "DIC_{TA}" denotes values calculated under the assumption that TA changed only due to crossover of conservative ions (i.e. K^+ and Cl^-), rather than OH^-, H^+, HCO_3^-, CO_3^{2-} or redox-active molecules. We calculated "DIC_{eq}" values assuming that gas-solution equilibrium was achieved at all states. The results are summarized in **Table S2** and **Figure S11**.

Table S2 Summary of pCO_2, pH, TA, DIC_{TA} and DIC_{eq} in concentrating cycle A and non-concentrating cycle B.

States	pCO_2(bar)	pH	TA (M)	DIC_{TA} (M)	DIC_{eq}(M)
$3'_{Ai}$	0.465	5.6	0.0066	0.0229	0.0229
1_A	0.465	7.1	0.1867	0.200	0.233
$1'_A$	1	6.8	0.1867	0.214	0.268
3_A	1	5.5	0.0067	0.0253	0.0475
$3'_{Af}$	0.465	5.8	0.0067	0.0167	0.0271
$3'_{Bi}$	0.465	5.8	0.0067	0.0167	0.0271
1_B	0.465	7.1	0.1867	0.199	0.233
$3'_{Bf}$	0.465	5.8	0.0067	0.0158	0.0280

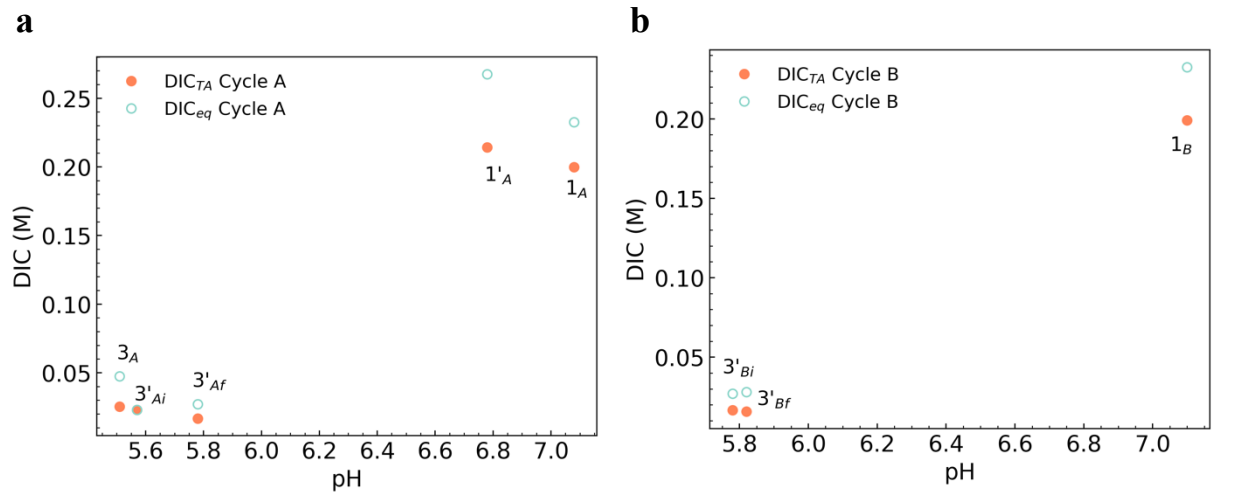

Figure S11 DIC versus pH in (a) concentrating cycle A and (b) non-concentrating cycle B.

Table S3 Summary of ΔDIC_{TA}, ΔDIC_{eq} , $\Delta DIC_{measured}$ and work input for different processes.

Process Nomenclature	Initial State	Final State	Process	ΔDIC_{TA} (M)	ΔDIC_{eq} (M)	$\Delta DIC_{measured}$ (M)	Work Input (J)
$\Delta DIC_{A3'1}$	$3'_{Ai}$	1_A	Deacidification/ Capture	0.177	0.210	NA	176.6
ΔDIC_{A13}	1_A	3_A	Acidification/ Release	-0.174	-0.185	NA	-73.8
$\Delta DIC_{A13'}$	1_A	$3'_{Af}$	Acidification/ Release	-0.183	-0.206	NA	-73.8
$\Delta DIC_{B3'1}$	$3'_{Bi}$	1_B	Deacidification/ Capture	0.182	0.206	0.186	173.5
$\Delta DIC_{B13'}$	1_B	$3'_{Bf}$	Acidification/ Release	-0.183	-0.205	0.190	-74.7

In concentrating cycle A, the amount of CO_2 captured at 0.465 bar is $\Delta DIC_{TA,A3'1}$, i.e. the difference between DIC values at $3'_{Ai}$ and 1_A, when no crossover of non-conservative ions is assumed, or $\Delta DIC_{eq,A3'1}$ when equilibrium is assumed. Neglecting the increment of CO_2 absorbed upon changing pCO_2 from 0.465 to 1 bar, the total amount of CO_2 captured at 0.465 bar and released at 1 bar is $\Delta DIC_{TA,A13}$ or $\Delta DIC_{eq,A13.}$, whereas $\Delta DIC_{TA,\ A13'}$ or $\Delta DIC_{eq,A13'}$ represent the sum of $\Delta DIC_{TA,A13}$ or $\Delta DIC_{eq,A13}$ and the amount of CO_2 released after pCO_2 is changed to 0.465 bar. In non-concentrating cycle B, the amount of CO_2 captured estimated from pH and TA is $\Delta DIC_{TA,B3'1}$ or $\Delta DIC_{eq,B3'1}$ and the amount of CO_2 released is $\Delta DIC_{TA,B13'}$ or $\Delta DIC_{eq,B13'}$. Because no transients occurred during non-concentrating cycle B, we also measured the amount of CO_2 captured or released via eq. 13 and denoted those values $\Delta DIC_{measured}$. **Table S3** summarizes ΔDIC_{TA}, ΔDIC_{eq}, $\Delta DIC_{measured}$ and work input, calculated using eq. 15, of the relevant processes. We note that $\Delta DIC_{measured}$ is on average only 3% higher than ΔDIC_{TA} but 8.5% lower than ΔDIC_{eq}; this result suggests that during non-concentrating cycle B crossover of non-conservative ions is insignificant. Note that $\Delta DIC_{TA,A13'}$ of concentrating cycle A is the same as $\Delta DIC_{TA,B13'}$ of non-concentrating cycle B, suggesting that the net amount of CO_2 released to 0.465 bar is the same whether it is released directly to a pCO_2 of 0.465 bar, or is first released to 1 bar before a pCO_2 of 0.465 bar is imposed. We expect less CO_2 to remain dissolved in solution after CO_2 release at a CO_2 partial pressure of 0.465 bar than after release at 1 bar; based on **Table S3**, 5–10% less CO_2 is released, depending on whether we assume full gas-solution equilibration or no crossover of non-conservative ions. For concentrating cycle A, the net cycle work is 102.8 J, which translates to 79.4 and 84.2 kJ/mol_{CO2} corresponding to ΔDIC_{TA} and ΔDIC_{eq}, respectively. For non-concentrating cycle B, the net cycle work is 98.8 J, which translates to 75.1 kJ/mol_{CO2}, using $\Delta DIC_{measured}$. Therefore, the work input for concentrating CO_2 from 0.465 to 1 bar is between 4.3 and 9.1 kJ/mol_{CO2} higher than that for CO_2 capture from and release to 0.465 bar. This value is two to five times higher than the limit from thermodynamic considerations (1.9 kJ/mol_{CO2}) but is small relative to our estimates of actual work input for CO_2 capture and release at 40 mA/cm^2, which range between 75.1 and 84.2 kJ/mol_{CO2}.

As mentioned in the **Discussion** section, part of the net cycle work overcomes cell overpotential, while the remainder is associated with CO_2 capture and release. We measured the former by cycling the same cell prior to cycles A and B under N_2 (i.e. no CO_2 capture and release)

at 40 mA/cm^2 and obtained a cycle work of 61.3 J. The difference between this figure and the cycle work in concentrating cycle A is 41.5 J, which, in combination with ΔDIC_{eq} or ΔDIC_{TA}, yields an actual work input dedicated only to CO_2 capture and release of 32.0 or 34.1 kJ/mol$_{CO2}$, respectively for an exit/inlet ratio 1/0.465.

5 *Estimate of Activation Overpotential*

The total cycle activation overpotential is the difference between deacidification overpotential and acidification overpotential, i.e.:

$$\eta_{total} = \eta_{deacidification} - \eta_{acidification} \quad eq.\ S\ 7$$

where $\eta_{deacidification}$ and $\eta_{acidification}$ each have cathodic and anodic components:

$$\eta_{cathodic} = \frac{RT}{\alpha nF} \ln \frac{i_0}{|i|} \quad eq.\ S\ 8$$

$$\eta_{anodic} = \frac{RT}{(1-\alpha)nF} \ln \frac{|i|}{i_0} \quad eq.\ S\ 9$$

where η is the activation overpotential, R is the ideal gas constant 8.314 J/mol K, T is the temperature 293.15 K and F is the Faraday's constant of 96,485 Coulomb/mol. α is the transfer coefficient of the redox couple, n is the number of electrons transferred per reactant molecule, i_0 is its exchange current density and i is the applied current. i_0 is calculated by:

$$i_0 = nAFk^0 Conc. \quad eq.\ S\ 10$$

where k^0 is the standard heterogeneous rate constant and Conc. is the concentration of the oxidized form of the electrolyte at 1:1 ratio of [oxidized form]:[reduced form], or a state of charge of 50%, and A is the electrode surface area, in our case 500 cm^2 for 4 sheets of SGL39 AA porous carbon paper electrodes, each of 5 cm^2 geometric surface area and 125 cm^2 surface area, assuming the specific area of SGL 39AA carbon paper is 0.5 m^2/g.[3]

For deacidification, the participating half reactions are :

Anodic: $Fe(CN)_6^{4-} \rightarrow Fe(CN)_6^{3-} + e^- eq.\ S\ 11$

Cathodic: $DSPZ + 2e^- + 2H_2O \rightarrow DSPZH_2 + 2OH^- \quad eq.\ S\ 12$

For acidification, the participating half reactions are:

Cathodic: $Fe(CN)_6^{3-} + e^- \rightarrow Fe(CN)_6^{4-} \quad eq.\ S\ 13$

Anodic: $DSPZH_2 + 2OH^- \rightarrow DSPZ + 2e^- + 2H_2O \quad eq.\ S\ 14$

Because the $Fe(CN)_6^{4-}/Fe(CN)_6^{3-}$ and DSPZ/$DSPZH_2$ redox couples are present in the posolyte and negolyte, respectively,

$$\eta_{deacidification} = \eta_{anodic,Fe} - \eta_{cathodic,DSPZ} \quad eq.\ S\ 15$$

$$\eta_{acidification} = \eta_{cathodic,Fe} - \eta_{anodic,DSPZ} \quad eq.\ S\ 16$$

For the DSPZ-containing negolyte, we estimated the activation overpotentials at the experimental currents of 200, 250, 375, 500, 625 and 750 mA based on $k^0 = 1.47 \times 10^{-2} cm/s$ and $\alpha = 0.4$, as reported by Xie *et al*, because of the similar structures of DSPZ and DHPS.[4] *Conc*. is 0.039 M at 50% state of charge and *n* is 2. The calculated i_0 for DSPZ/DSPZH$_2$ is 55 mA. The resulting $\eta_{cathodic,DSPZ}$ at the experimental currents are –41, –48 , –60, –70, –77 and –82 mV, respectively and $\eta_{anodic,DSPZ}$ at the experimental currents are 27, 32, 40, 46, 51 and 55 mV, respectively. For the posolyte side, we estimated the activation overpotential using reported ferrocyanide/ferricyanide $k^0 = 1.5 \times 10^{-2}$ cm/s and $\alpha = 0.5$ reported by Angell *et al*.[5] *Conc.* is 0.1 M at 50% state of charge and *n* is 1. The calculated i_0 for $Fe(CN)_6^{4-}/Fe(CN)_6^{3-}$ couple is 72 mA/cm^2. The resulting $\eta_{anodic,Fe}$ at the experimental currents are 51, 63, 83, 98, 109, and 118 mV, respectively and the resulting $\eta_{cathodic,Fe}$ at the experimental currents are –51, –63, –83, –98, –109, and –118 mV, respectively. These values and the corresponding $\eta_{deacidification}$ and $\eta_{acidification}$ values are summarized in **Table S 4**.

Table S4. Estimated activation overpotentials at various currents*

Current/Components	200 mA	250 mA	375 mA	500 mA	625 mA	750 mA
$\eta_{anodic,Fe}$	51	63	83	98	109	118
$\eta_{cathodic,DSPZ}$	–41	–48	–60	–70	–77	–82
$\eta_{deacidification}$	92	110	144	167	185	200
$\eta_{cathodic,Fe}$	–51	–63	–83	–98	–109	–118
$\eta_{anodic,DSPZ}$	27	32	40	46	51	55
$\eta_{acidification}$	–78	–95	–123	–144	–160	–173

*Units in mV

Using $\eta_{deacidification}$ and $\eta_{acidification}$ values with absolute values above 118 mV, we linearly extrapolate to zero current and obtain an η_{total} of 165 mV.The electrical work associated with the cell activation overpotential is

$$w = \eta_a q, \quad eq.\ S\ 17$$

where *q* is the cell capacity required for capturing/releasing 1 mol CO_2 and can be calculated by

$$q = \frac{nF}{r}, \quad eq.\ S\ 18$$

where *r* is the ratio of ΔDIC to DSPZ concentration (in this case 0.158/0.078 because 0.078 M DSPZ was able to capture enough CO_2 to make a solution with 0.158 M ΔDIC), and *n* = 2 because DSPZ undergoes a 2-electron process. We obtained a cell capacity of 140000 C and an electrical work of 15.7 kJ/mol$_{CO2}$.

Note that deviations from this value could take place because of several factors including but not limited to:

1. The rate constants were measured with glassy carbon or metal electrodes whereas carbon paper electrodes were used in the experiments;
2. The rate constants were measured in a solution with no anti-foam agent whereas anti-foam agent was present in the experiments;

3. The rate constants were measured at a specific pH whereas the experiments covered a range of pH values;
4. Based on the large peak separation displayed on the CV diagrams (**Figure 8**c), DSPZ is likely to have more sluggish kinetics and hence possess a smaller rate constant than DHPS. In order for the estimate above to yield 32 kJ/mol$_{CO2}$ electrical work instead of 15.7 kJ/mol$_{CO2}$, the kinetic constant of DSPZ would have to be ~ 1×10^{-4}cm/s, which is a reasonable value compared to the rate constants of other organic redox active molecules used in a flow cell;
5. The electrode active area was calculated based on previous literature[3], but different electrode pretreatment could result in different active area.

6 Estimate of CO_2 Kinetic Losses

The ideal cycle work for the four-process CO_2 separation cycle depends on the exit/inlet pressure ratio (p_3/p_1) and the CO_2 outgassing overpressure (p_2/p_3)(**Figure 7**). For the experimental conditions outlined in **Figure 10**, the exit/inlet pressure ratio for absorbing CO_2 from a gas stream with 0.465 bar CO_2 partial pressure and release to 1.0 bar CO_2 is 2.17. The CO_2 outgassing overpressure is 5.54 if [CO_2 (aq)] after acidification is 0.159 M. Using these values and the same program that generated **Figure 7**, we obtain an ideal cycle work of 34 kJ/mol$_{CO2}$.

This calculation, however, assumes a four-process CO_2 separation cycle from 0.1 to 1 bar CO_2(g), whereas the experimental situation is arguably closer to the two-process CO_2 separation cycle shown by the dashed lines in **Figure 5** and **Figure 6**. A definition of the minimum electrochemical work that is readily applicable to these experimental conditions is the sum of the CO_2 kinetic losses, i.e. exergetic losses during CO_2 release and invasion, and the thermodynamic minimum work of separation. The total exergy lost during CO_2 release can be estimated as:

$$\overline{w} = RTln\frac{[\widetilde{CO}_2(aq)_{release}]}{[\,CO_2(aq)_{equilibrium}]} \quad eq.\ S\ 19$$

where $[\widetilde{\mathrm{CO}}_2(\mathrm{aq})_{\mathrm{release}}]$ is the average aqueous CO_2 concentration during outgassing, and $[\,\mathrm{CO}_2(\mathrm{aq})_{\mathrm{equilibrium}}]$ is the CO_2 concentration in local equilibrium with the head space, which in this case is the product of 0.465 bar and the Henry's Law constant of 3.5×10^{-2} mol/(L bar), which yields 0.016 M. In the limit where the flow of gas in the cell headspace is infinitesimal, the increase in $[\mathrm{CO}_2(\mathrm{aq})]$ above its steady-state value (e.g., in **Figure 10**) is proportional to the increase in CO_2 partial pressure in the headspace, i.e.

$$\Delta[CO_2(aq)] = \frac{\Delta p_{co2}}{RT}\frac{V_{headspace}}{V_{electrolyte}} \quad eq.\ S\ 20$$

where Δp_{co2} is the change in partial pressure of CO_2 in the headspace during CO_2 invasion or release, $V_{electrolyte}$ is the volume of the electrolyte (7 mL) and $V_{headspace}$ is the volume of the headspace (~ 50 mL). The average Δp_{co2} during CO_2 outgassing was 0.05 bar (**Figure 10**e) resulting in a $[\widetilde{\mathrm{CO}}_2(\mathrm{aq})_{\mathrm{release}}]$ of 0.031 M (i.e. 0.016 M + 0.015 M), and $\overline{w}$ of 1.6 kJ/mol$_{CO2}$. This figure, however, is an estimate of the lower limit of the exergy lost, as the flow rate of gas in the cell headspace is finite, and the measured $\Delta\mathrm{p}_{\mathrm{co2}}$ would therefore be lower than that for the infinitesimal-flow limit for the same $\Delta[\mathrm{CO}_2(\mathrm{aq})]$. We estimate the upper limit of the exergy lost

by assuming that the increase in [CO_2(aq)] is equal to the DIC increase during CO_2 invasion, i.e. that all CO_2 that came in during invasion is present as supersaturated CO_2 before outgassing begins. Under these conditions, the numerator in eq. S19 is 0.159 M + 0.016 M, and the corresponding lost exergy is 5.8 kJ/mol$_{CO2}$. A reasonable estimate for the lost exergy is the average of the two estimates, which is 3.7 kJ/mol$_{CO2}$.

The exergy lost during CO_2 invasion, on the other hand, is the maximum amount of work that can be recovered from the reaction between OH^- and CO_2, and is the absolute value of the Gibbs free energy of the reaction, ΔG_R. In the present case,

$$\Delta G_R = \Delta G_R^O + RT ln\, N, \quad eq.\ S\ 21$$

where

$$\Delta G_R^O = -RT \ln K_{eq}; \quad eq.\ S\ 22$$

K_{eq} is the equilibrium constant, and N is the average reaction quotient during CO_2 invasion. ΔG_R is therefore equal to $RT \ln (N/K_{eq}) . N/K_{eq}$ is proportional to the ratio between the OH^- and aqueous CO_2 concentrations at equilibrium (i.e. 3.16×10^{-8} and 0.016 M), and the average OH^- and CO_2 concentrations during CO_2 invasion, $[\widetilde{CO_2}(aq)_{invasion}]$, which can be derived from pH measurements, and the relationship between Δp_{co2} and $\Delta[CO_2(aq)]$ shown above, respectively. Given an average [OH^-] during invasion of 2.5×10^{-6} M and average CO_2 partial pressure during invasion of 0.42 bar, $[\widetilde{CO_2}(aq)_{invasion}]$ is 0.003 M (= 0.016 M – 0.013 M) and the corresponding exergy lost during CO_2 invasion is 6.6 kJ/mol$_{CO2}$ (**Figure 10**d and e). Because the thermodynamic minimum work of separation is zero here, the minimum electrochemical work input would be 10.3 kJ/mol$_{CO2}$.

Our estimate of the minimum electrochemical work input could be off because:

1. The average aqueous CO_2 concentration, instead of instantaneous CO_2 concentration, was used in the calculation;
2. Exergy losses are nonlinearly related to concentration;
3. The ratios $[\widetilde{HCO_3^-}_{invasion}]/[HCO_3^-{}_{equilibrium}]$ and $[\widetilde{CO_3^{2-}}_{invasion}]/[CO_3^{2-}{}_{equilibrium}]$ may deviate significantly from 1, as is implicitly assumed here.

Note that the above calculations neglect exergy losses from mixing between absorbed or released CO_2 and the 0.465 bar CO_2 reservoir, as these are external to the device itself.

7 Bibliography

1. K. Lin, Q. Chen, M. R. Gerhardt, L. Tong, S. B. Kim, L. Eisenach, A. W. Valle, D. Hardee, R. G. Gordon, M. J. Aziz and M. P. Marshak, *Science*, 2015, **349**, 1529.
2. C. Costentin, *Chem. Rev.*, 2008, **108**, 2145-2179.
3. A. Forner-Cuenca, E. E. Penn, A. M. Oliveira and F. R. Brushett, *Journal of The Electrochemical Society*, 2019, **166**, A2230-A2241.
4. H. Xie, Y. Wu, T. Liu, F. Wang, B. Chen and B. Liang, *Applied Energy*, 2020, **259**, 114119.
5. D. H. Angell and T. Dickinson, *J Electroanal Chem*, 1972, **35**, 55-72.